DEPARTMENT OF PHYSICS
UNIVERSITY OF JYVÄSKYLÄ
RESEARCH REPORT No. 6/2007

NUCLEAR MICROSCOPY: DEVELOPMENT AND APPLICATIONS IN ATHEROSCLEROSIS, PARKINSON'S DISEASE AND MATERIALS PHYSICS

by
Ren Min-Qin

Academic Dissertation
for the Degree of
Doctor of Philosophy

To be presented, by permission of the
Faculty of Mathematics and Natural Sciences
of the University of Jyväskylä,
for public examination in Auditorium FYS-1 of the
University of Jyväskylä on Nov 16, 2007
at 12 o'clock noon

Jyväskylä, Finland
Nov 2007

ISBN 978-951-39-3186-5
URN:ISBN:978-951-39-3186-5

Preface

The realization of this thesis wouldn't have been possible without the help of many people. I would like to express my deep gratitude to some of them by name, with my apologies for possible omissions . . .

I would like to thank Professor *Frank Watt* for giving me the opportunity to work in the Center for Ion Beam Applications (CIBA) group at the National University of Singapore (NUS). He has been the most excellent mentor for many years in all the research work I've been doing. Most important has been his ability in being able to create such a wonderful group for all of us to have the joy of doing research under his leadership.

Professor *Harry J Whitlow* has been such an enthusiastic visiting professor at CIBA, he has been my bridge to the University of Jyväskylä in Finland and he has since become a great mentor for my study and research work. I thank him for making the PhD program possible for me and also giving me the opportunity to be a PhD student at Jyväskylä University and experience the goodness and well-being of the Finnish society.

Associate Professor *Thomas Osipowicz*, his excellent lectures on *Nuclear physics* and *Accelerator based materials characterization techniques* have greatly strengthened my understanding of the research topics discussed in this thesis. I need to thank him for the meaningful discussions when I was dealing with the calculation of lateral and angular scattering of light ions penetrating biological materials. He has been a great mentor in many ways.

Professor *Barry Halliwell*, it's been a great honor to work for the projects headed by him and all the valuable scientific discussions with him.

Assistant Professor *Jeroen van Kan* has given excellent technical help during many of my experiments. He has been such a kindhearted colleague to share an office with and most importantly for being a good friend throughout the years.

Associate Professor *Mark Breese*, for his invaluable help, advice and continuous encouragement.

Dr *Reshmi Rajendran*, my 'biomedical' team-mate in CIBA; whenever a problem occurs, she is the first one I think of to discuss with. I would also like to thank her for introducing LaTeX program to me in such a simple and fun way, which greatly shortened the time I would have taken to overcome the fear of using this program described by many people . . . At this point, I would also like to acknowledge Dr *Chammika Udalagama* for getting the LaTeX program started and running properly on my computer.

Assistant Professor *Andrew Bettiol* is thanked for all his help especially his ability to recover many of my files that "disappeared", and Dr *Teo Ee Jin* for sharing her thesis, which was a good reference to understand LaTeX better.

I wish to thank *Zhang Fang*, *Wang Liping* and my special friend in Belgium *Elisabeth Wieslander* for all the cheerful moments that we have spent together in work and free time.

I wish to thank the accelerator *guru* Mr *Choo Theam Fook* in CIBA for his technical support in keeping the accelerator in good condition.

I extend my thanks to all the people in the Department of Physics in Jyväskylä University, especially Professor *Rauno Julin* and Associate Professor Timo Sajavaara for their help in the course of my PhD studies.

I also thank all the other members in CIBA group; they have all helped me in one way or another, and I'm very grateful to all of them.

I thank all my collaborators for their important contributions to my publications, especially Associate Professor *Bay Boon Huat* and his group for their great help in the *Nano-STIM* work.

I would also like to thank the Finnish Graduate School in Particle and Nuclear Physics for the financial support during this PhD programme.

Finally, my family, especially my parents, my husband Dr *Du Quangang* and our two beloved daughters *Yiran* and *Yilin*. I really appreciate their constant love and continuous support.

Last, but not least, Miss *Rio Grace Manual*, my great helper at home; you've done much more than you'll ever imagine to the family, especially for me to have the huge amount of time required for this thesis!

Singapore,
May 2007

Ren Minqin

任閩秦

Abstract

Nuclear Microscopy is a powerful set of nuclear based techniques which are proving to be very useful in the field of life sciences. With the ability to focus MeV ion beams down to sub micron spot sizes, the Nuclear Microscopy facility in the National University of Singapore (NUS) has the best performance worldwide, and with the finely tuned combination of Particle Induced X-ray Emission (PIXE), Rutherford Backscattering Spectrometry (RBS) and Scanning Transmission Ion Microscopy (STIM), it enables us to image the morphology of biomedical tissue (and cells), map trace elements like Ca, Fe, Cu and Zn, etc and measure them down to the parts per million level.

The goal of the research programs involved in this thesis is to apply the nuclear microscopy method for quantitative biomedical and materials analysis. One of the greatest values of Nuclear Microscopy is the capability to obtain truly quantitative composition data. However, the inhomogeneity and liability of biomedical samples presents a challenge to achieve this.

The work described in this thesis focuses on quantitative analysis of biomedical and materials using nuclear microscopy techniques. The biomedical applications are carried out on two major age-related diseases - atherosclerosis and Parkinson's disease. Work involving quantitative parameterisation of the thickness distribution of cells and lithographically defined stopping media for fundamental stopping force measurements is also described.

Abstract in Chinese

随着近代科学技术的发展和人们对微观物质表面形态，化学组成和空间结构研究的需要，各种显微分析技术得到了迅速发展，这些技术的发展又推动了基础研究的进步。四十多年来电子微束技术的发展对生物学，医学，材料科学和地学等领域都产生了深刻的影响。而近年来不断出现的其他微束分析技术（激光微束，离子微束，X 射线微束）也正进一步拓宽人们对微观世界的认识。 核子微探针 (Nuclear Microprobe）就是其中之一。

核子微探针是利用加速器产生能量为 MeV 的质子或其他粒子，经准直，聚焦为可进行扫描的微束，并用其激发在光学显微镜下所选微区的待分析物质（靶）， 然后借助相应的探测器接受微束与物质相互作用所产生的多种信息（比如：特征 X 射线，γ 射线，背散射粒子和次级电子等等），经计算机和信号采集系统采集，储存和处理，来研究微区内物质的表面形态，化学组成及元素的空间分布等。Cookson 等人曾全面评述了这一技术的早期工作和进展。

自 1972 年世界上第一台核子微探针在英国 Harwell 问世以来，许多原来用于核物理研究的小型加速器相继增添了各种类型的核子微探针，并迅速发展成为一门十分重要的现代核分析技术。为了满足细胞水平元素分布分析的要求，分析仪器必须具备亚细胞水平的空间分辨本领。新加坡国立大学核子显微镜中心（Center for Ion Beam Applications）的核子显微镜设备目前在本领域内处于世界领先水平，空间分辨率的最新纪录是在 2007 年 5 月所达到的 30 x 40 nm。根据计算，在最理想的条件下，离子束的空间分辨率可达 5 nm。

核子微探针技术可分为基于离子数目测量的显微分析技术和基于离子束能量测量的显微成像技术，表 1 列出了各种核子微探针所采用的离子束与物质的相互作用及相关的核技术。一台性能优良的核子微探针，应能在一次实验中综合使用多种核效应，以同时获得微区结构内的多重信息包括样品密度、形态和元素含量的三维分布图。

表 1　现代核子微探针技术

相关技术(代号)	**相互作用方式**	**首次应用**
二次电子成像 (SEI)	二次电子和 Auger 电子发射	1972
粒子激发 X 射线荧光 (PIXE)	X 射线发射	1976
卢瑟福背散射 (RBS)	背散射	1977
核反应分析 (NRA)	核反应	1977
弹性反冲分析 (ERDA)	弹性反冲	1983
沟道反差显微术 (CCM)	沟道效应	1983
卢瑟福前散射 (RFS)	前向散射	1985
扫描透射显微术 (STIM)	能量损失	1987
离子束光刻术 (IBL)	辐射损伤	1987
离子束感生电荷 (IBIC)	电子-空穴对产生	1989
扫描透射沟道显微术 (CSTIM)	沟道效应	1991
离子束显微拓扑学 (IMT)	表面拓扑	1991
离子荧光显微成像 (IL)	可见光发射	1992

目前核子微探针所用质子束能量多在 0.5 --- 8 MeV 之间，空间分辨率可达 0.1 --- 1 μm，分析元素范围可涵盖整个元素周期表，这当然取决于在测量过程中所用到的探测器和相关的数据采集系统。元素的检测限可达百万分之一的量级 (ppm)，并可获得选区的光学图像，背散射图像和各元素的空间分布图。

本论文中所要阐述的科研课题是在新加坡国立大学核子显微镜中心完成的。

新加坡国立大学核子显微镜实验室有具备世界一流水平的核探针系统。这个核探针系统的主要设备有：加速器，离子源，质子束准直和聚焦系统，靶室，各种探测器，计算机控制和数据处理系统。三条束流传输系统：第一条（10° beam line）主要是用于对纳米材料和纳米结构的研究和开发，第二条（30° beam line）

主要是用于材料科学和生物医学研究，第三条（45° beam line）是应用高分辨率（0.3 nm）卢瑟福背散射方法对材料的表面性能做精确的研究。

本论文中主要用到的核分析技术有：1. 质子激发 X 射线荧光 (PIXE)，此项技术利用 X 射线的特征谱可提供元素含量及其分布的信息；2. 卢瑟福背散射 (RBS)，此项技术通常用于材料分析。在分析很薄的生物组织切片时，RBS 可以提供基体特征如厚度、密度和 C、O、N 等轻元素的信息； 3. 扫描透射粒子显微镜（STIM）可提供形貌(结构)信息。在大多数情况下，为了防止扫描透射粒子显微镜的探测器被意想不到的强束流破坏，所用到的探测器都是被置放于偏离束流 20° 的方向 。这三项技术可以同时使用来对所研究的材料进行定性和定量分析。这些技术的另外一个重要的优点就是无损分析，因此可在当代许多科学领域如生物，医学，材料，地学，冶金，环保和考古等众多学科中发挥重要作用。

本论文的主要内容就是对以上所提到的三项核技术在生物医学研究中应用的可行性和相关的技术应对措施进行探讨。论文中所涉及到的医学课题主要有：

1．心血管疾病 --- 动脉粥样硬化 (Atherosclerosis)
2．帕金森氏综合征 (Parkinson’s disease)

动脉粥样硬化是一种以器官或组织供氧不足为特征的病理学过程，用特异染色法或组织学方法很难检测动脉壁的早期变化，但应用核子微探针技术则有可能通过观察动脉壁不同细胞层和不同结构中的元素谱变化了解宏量元素和微量元素在病理发生学中的作用。我们在动脉粥样硬化动物模型中观察到，损伤的动脉组织中铁（Fe）的含量比邻近血管壁组织增加了 7 倍。这一结果有力地支持了动脉粥样硬化的低密度脂蛋白(LDL)氧化变性假设：LDL 在动脉壁中受到氧化变性，变性后的 LDL 对内皮细胞 (endothelial cells) 有毒。在被巨噬细胞 (macrophages) 吞噬变性后的 LDL 会形成泡沫细胞 (foam cells)，后者是动脉粥样硬化损伤的前体。论文中相关的章节对动物模型，喂养方法，样品采集，样品处理和数据分析都有详细地探讨和说明。

帕金森氏病（PD）是一种主要影响运动的进行性发展的神经系统疾病。虽然帕金森氏病更常见于老年人，但也有些人在 40 岁之前就开始出现症状（如肌强直或肌僵直，震颤，动作减慢和平衡及行走障碍）。经过多年来的大量研究，现已基本明确，帕金森氏病是由脑组织中神经递质多巴胺（dopamine）缺陷引起的，它与脑中黑质区(Substantia Nigra)产生多巴胺的细胞缺损有关。虽然该病的许多特征，如线粒体功能、铁代谢和谷胱甘肽水平的变化，已经得到证实，但导致多巴胺细胞死亡的原因仍不清楚。我们通过注射神经毒素MPTP使猴子（primates）产生帕金森氏病, 综合应用多种核子微探针技术(micro-PIXE, RBS和STIM) 测定老猴子和小猴子脑中黑质区的元素分布，发现老猴子大脑黑质中的Fe的平均水平是1092 ppm, 而小猴子大脑黑质中的Fe水平是233 ppm, 区别相当明显。在比较损伤一侧和非损伤侧大脑黑质中的Fe水平后发现在老猴子的脑中，损伤一侧比非损伤侧大脑黑质中的Fe水平增加了10%。而小猴子的则没有明显的区别。另外一个重要的结果就是直接在染色（神经元细胞染色）的组织上进行微束扫描来对比元素分布和神经元细胞分布的关系，研究结果发现无论在老猴子还是在小猴子的脑中，在Fe集中的地区神经元细胞的数量明显的减少，这一现象在老猴子的脑中尤为显著。Fe可诱发催化氧化反应，产生自由基，因而我们的研究结果支持帕金森氏病与自由基产生有关的假设。详细内容见本论文的第五章。

鉴于其他脑病(例如，进行性核上麻痹、多发性全身萎缩、阿尔采默病、多发性硬化等)也出现 Fe 水平增高现象，因而脑中黑质区中 Fe 水平增加是帕金森氏病的病因还是继发结果尚有待进一步研究。

综上所述，核子微探针的发展使生命科学中微量元素研究能在细胞水平上测量生物组织中元素分布的研究成为可能。

Publication list

This thesis is based on the following publications (my contributions are in parentheses):

1. *Iron concentrations and distributions in the parkinsonian substantia nigra of aged and young primate models.* **MQ Ren**, JP Xie, XS Wang, WY Ong, SK Leong, F Watt, Nucl. Instr. Meth. B *181*(1-4), 522-528, (2001). (Post mortem sample preparation, nuclear microscopy measurements and data analysis, principal author.)
2. *A nuclear microscopy and histochemical study of iron concentrations and distribution in the midbrain of two age groups of monkeys unilaterally injected with MPTP.* **MQ Ren**, WY Ong, AS Wang, F Watt. Experimental neurology, *184*(2), 947-954, (2003). (Post mortem sample preparation, analyzed the stained sections on pioloform film using both optical microscopy and nuclear microscopy to correlate the distribution of neuronal bodies and iron granules, data analysis, principal author.)
3. *Trace elemental distributions in induced atherosclerotic lesions using nuclear microscopy*, **Ren Minqin**, F Watt, B Tan Kwong Huat, B Halliwell. Nucl. Instr. Meth. B *210*(September), 336-342, (2003). (Took part in planning the project, sectioned and prepared the samples on pioloform, carried out the nuclear microscopy measurements and data analysis, principal author.)
4. *Correlation of iron and zinc with lesion depth in newly formed atheriosclerotic lesions.* **Ren Minqin**, Frank Watt, Benny Tan Kwong Huat and Barry Halliwell. Free Radical Biology and Medicine, Vol. *34(6)*, 746-752, (2003). (Took part in the preparation of the protocol, took part in the blood sample analysis, prepared the samples, carried out the nuclear microscopy measurements, lesion area analysis using image analyzer and data analysis, principal author.)
5. *The iron chelator desferrioxamine inhibits atheriosclerotic lesion development and decreases lesion iron concentrations in the cholesterol-fed rabbit.* **Ren Minqin**, R Rajendran, N Pang, B Tan Kwong Huat, WY Ong, F Watt and B Halliwell. Free Radical Biology and Medicine, *38*(8), 1206-1211, (2005). (Took part in the preparation of the protocol, prepared the samples, carried out the nuclear microscopy measurements and data analysis, principal author.)
6. *Measurements of the stopping forces for heavy ions in Ge, Ag and Au using novel 'polka-dot' detectors.* TDM Weijers-Dall, H Timmers, K Stenström, P Persson, A Pergjegjaj, X Wang, M Graczyk, T Osipowicz, **MQ Ren**, DJ O'Connor, and HJ Whitlow. Nucl. Instr. Meth. B *251*(2), 352-360, (2006). (Carried out the RBS measurements on the stopping medium coated polka-dot samples for the determination of the stopping force.)

7. *Nano-imaging of single cells using STIM.* **Ren Minqin**, JA van Kan, AA Bettiol, Lim Diana, Chan Yee Gek, Bay Boon Huat, HJ Whitlow, T Osipowicz and F Watt. Nucl. Instr. Meth. B *260*, 124-129, (2007). (Led the preparation of the experimental protocol, carried out part of the sample preparation, carried out NM measurement and necessary calculations.)

8. *Exploratory nuclear microprobe data visulisation using 3- and 4- dimensional biological volume rendering tools.* Harry J Whitlow, **Minqin Ren**, Jeroen van Kan, Frank Watt and Dan White. Nucl. Instr. Meth. B *260*, 28-33, (2007). (Took part in the sample preparation, carried out the nuclear microscopy measurement and contributed to writing the paper.)

9. *Rugged figures of merit for focusing MeV ion beams in proton beam writing and imaging.* **Minqin Ren**, Harry J Whitlow and Ananda Sagari A.R. Submitted to Journal of Applied Physics. (Took part in the nuclear microscopy measurements, some data analysis and the calculations, contributed to writing the paper.)

Contents

1 Introduction

1.1 The overall view

The study of life processes shows that many vital functions depend on the presence of a specific essential trace element. The simplest definition of an essential trace element is that it is required in small amounts for the maintenance of life; its absence results in death or a severe malfunction of the organism.

Of all the 90 naturally occurring elements, 26 are known to be essential to animal life. Amongst these 26 elements, iron (Fe), copper (Cu), zinc (Zn), manganese (Mn), nickel (Ni), cobalt (Co), molybdenum (Mo), selenium (Se), chromium (Cr), iodine (I), fluorine (F), tin (Sn), silicon (Si), vanadium (V) and arsenic (As) are trace elements. The other 11, namely, carbon (C), hydrogen (H), oxygen (O), nitrogen (N), sulfur (S), calcium (Ca), phosphorous (P), sodium (Na), chlorine (Cl) and magnesium are major elements in biological systems.

Most of the trace elements serve a variety of functions, depending upon their chemical form or combination and their location in the body tissues and fluids. Minor and trace elements serve two general roles. The first one is their function as structural material. For example, iron is part of the structure of the oxygen-carrying protein, haemoglobin, in the red blood cells; calcium, phosphorus and other elements constitute a significant part of the mass of teeth and bones; and sodium, potassium, phosphate, sulfate, chloride and many other elements are important constituents of the fluids, both inside and outside all the body cells. The second general role of trace elements is their function in regulating numerous biological activities. For example, calcium in minute concentrations is necessary for normal blood clotting; magnesium stimulates the activity of many enzymes and a number of trace elements control the contraction of muscle tissue and the transmission of impulses by nerve cells.

Trace elements are processed and stored in biological compartments on different scales; their concentration varies from 1 atom per protein molecule to 30% Ca in bone. An excess or imbalance of these elements has been implicated in the pathogenesis of several age-related diseases, for example, Parkinson's disease and atherosclerosis.

Therefore, the development of techniques which can accurately measure trace elements, is important. Nuclear microscopy utilizes a variety of high energy (MeV) ion beam techniques at sub-micron spatial resolutions to provide elemental imaging (shown in Figure 1.1) and quantitative elemental analysis of biological tissue down to the parts per million (ppm) level of analytical sensitivity. The techniques used in this thesis are Particle Induced X-ray Emission (PIXE), Rutherford Backscattering Spectrometry (RBS) and Scanning Transmission Ion Microscopy (STIM). These three techniques, which can be carried out simultaneously, are extremely useful for mapping and measuring the concentrations of major, minor and trace elements in biological tissues [Watt95, Ong99, Ren99, Thon99]. The measurement of elemental distributions within the cells and the tissues on a micrometer scale (or even $\sim$ 100 nm scales) can contribute to the knowledge of the different stimuli in which the trace element may play a very important role.

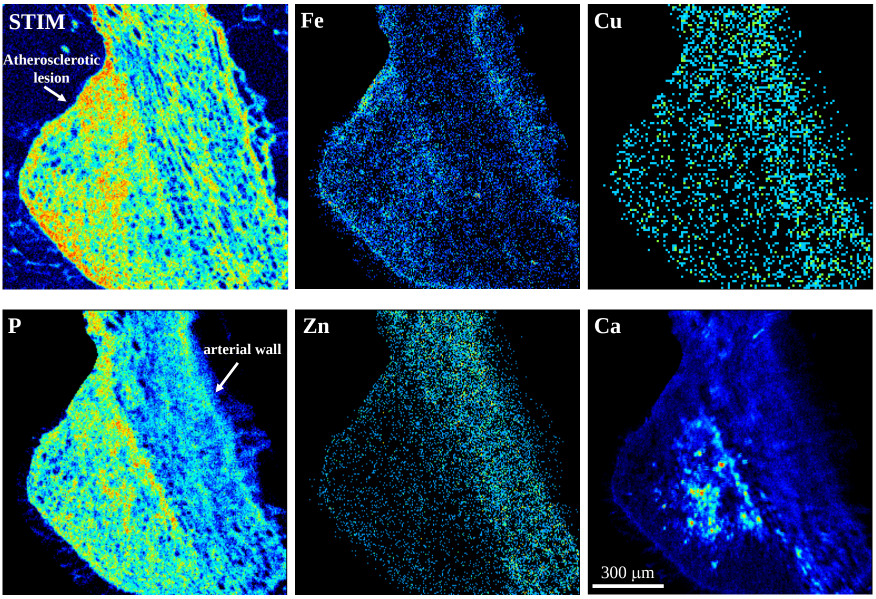

Figure 1.1: STIM and elemental maps obtained simultaneously during Nuclear Microscopy measurement (shown in picture is a 16 μm thick section of aorta from a New Zealand white rabbit fed for 8 weeks on a high fat diet (1% cholesterol). In this example, the atherosclerotic lesion is not uniform around the artery wall, but protrudes from the artery wall. The lesion is delineated by the off-axis STIM image (higher density) and P map).

1.2 Synopsis

A brief overview of the nuclear microprobe facility at the Centre for Ion Beam Applications, including beam line and its various components as well as their functions is given in chapter 2. In this chapter, the relevant analytical techniques and the principles behind them are introduced. Chapter 3 discusses investigations of the factors limiting the resolution for biomedical specimens.

Applications of nuclear microscopy techniques are explored in chapters 4 to 6. We have focused on a few important physical topics in developing the method to solve some particular issues in our work. Chapters 4 and 5 describe the biomedical applications using our nuclear microprobe, and chapter 6 presents some applications in materials physics.

Chapter 4 describes the role of trace elements in one of the age-related diseases – atherosclerosis. The experiments were conducted on New Zealand white rabbits fed a high fat diet to induce atherosclerosis. The results show that the development of atherosclerotic lesion is strongly correlated with the iron concentration and inversely correlated with the zinc concentration. Our data add support to the view that iron may be a promoter of atherosclerosis through iron mediated free radical catalysis, and zinc may have an antiatherosclerotic effect.

Chapter 5 presents the study carried out on another age-related disease – Parkinson's disease. In this chapter, a special Nissl staining procedure for staining brain sections on *pioloform* film (the procedure for making this film can be found in Appendix A) coated nuclear microscopy target holders has been introduced. MPTP-induced hemiparkinsonian primates were used as animal models, the non-lesioned substantia nigra (SN) served as controls. The most interesting observation of this study is the inverse correlation between the iron-rich granules and the distribution of intact neurons especially in old primates. The results may implicate iron as a factor in dopaminergic cell death through iron-catalyzed free radical production, which support the theory that iron-mediated oxidative stress may be involved in Parkinson's disease.

In chapter 6, some aspects of quantitative nuclear microscopy in materials physics research are investigated. Si PIN diodes have been employed through this work for different purposes - as STIM detector, substrate for growing cells and coated directly with a patterned layer of the stopping medium for the measurement of stopping force of different materials.

Final conclusions and future aspects of nuclear microscopy techniques are given in chapter 7.

1.3 Ethical considerations

Prior to starting the animal experiments, ethical approval was obtained from the local Animal Care and Use Committee of the National University of Singapore. The relevant work was carried out in accordance with the legislation of the Republic of Singapore. Procedures using animals were conducted by qualified veterinary surgeons and technicians.

2 Facilities and analytical techniques

2.1 The Nuclear Microprobe

Figure 2.1 illustrates the set-up of the CIBA nuclear microprobe in the National University of Singapore [Watt03]. The set-up consists of a 3.5 MV high brightness High Voltage Engineering Europa Singletron^{TM} ion accelerator, three state-of-the-art beam lines — the proton beam micro-machining line, the nuclear microscope line and the high resolution RBS/channeling facility line. These systems are normally maintained under a vacuum level of 10^{-6} mbar by means of magnetically levitated turbo molecular pumps. (Figure 2.1).

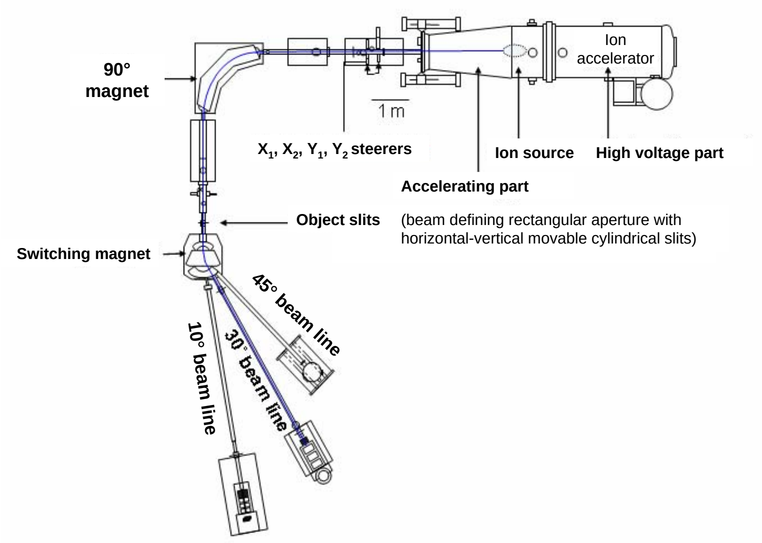

Figure 2.1: The setup of CIBA nuclear microprobe (30^o), P-beam writing (lithography) (10^o) and high resolution RBS/Channeling (45^o) beam lines.

The setting up of the nuclear microprobe starts from ion source, which is a key part of any Ion Beam Application (IBA) facility. The special demands on the ion source for nuclear microprobe applications are high beam brightness, high stability and a long lifetime. Protons and alpha particles are the most frequently used particles in the single-ended accelerator. The ion source types frequently used are *R.F.* gas source and the duoplasmatron. The *R.F.* gas source in the CIBA accelerator works satisfactorily with a large output current, the drawback being that of limited beam brightness. The CIBA ion source is fed from a number of source bottles which contain hydrogen and helium gas. The gas is excited by a radio-frequency field of 125 MHz generating either hydrogen or helium ions. The ions are then accelerated through a tube which is a succession of cylindrical electrodes allowing the beam to pass through. The high voltage required is generated by a series of solid state rectifiers based on the Cockcroft Walton principle.

The size of the beam is defined by two sets of precision slits made from tungsten carbide roller bearings. The first slits are the object slits, defining the beam size for pre-focusing and the collimated slits are the second slits, which define beam divergence. The adjustment range of the objective and collimated slits should be from zero to a few hundred μm for the different demands on beam conditions made by different techniques. For instance, PIXE and RBS usually need beam currents of about 100 pA to a few nA or larger, whereas STIM (especially on-axis STIM) may only need about 0.1 fA for performance with a high spatial resolution. The setting of the slits usually involves a compromise between reasonable beam current and beam size. Small beam size is usually achieved at the expense of a very low beam current.

	Nuclear Microscopy	P-Beam Writing
Beam line	30^o	10^o
Quadrupole lenses	OM 50 triplet	OM 52 triplet
Object slits to lens distance	6.4 m	6.4 m
Beam focus to lens distance	16 cm	7 cm
D_x	88	228
D_y	24	60
Beam spot	500 nm $\sim$ 1 μm	35 × 75 nm
Beam current	0.1 $\sim$ 500 nA	1.6 fA to 10 pA

Table 2.1: Basic parameters of the Nuclear Microprobe beam lines used for the research work carried out in this thesis.

The key part with regard to the beam size in a nuclear microprobe is the probe-forming lens system. The lens can be of electrostatic or magnetic quadrupole type (we need to bear in mind that the magnetic deflection depends on momentum/q, and is therefore mass dependent whereas electrostatic deflection depends on energy/q, and is therefore independent of mass). The lens system can be a configuration of quadruplet, triplet or doublet [Grim84]. Basic features of the CIBA nuclear microprobe beam lines employed for the research work carried out in this thesis are summarized in Table 2.1 [Watt03].

The data signals are processed by a data acquisition system OMDAQ [Grim91], which stores the amplitude of every event detected from the sample, along with its spatial coordinate. This is widely known as the list-mode data acquisition. The advantage of this event-to-event scheme is that all signals from the detectors are recorded, which allows the experiment to be replayed at the conclusion of data taking. This is useful for biomedical work, where many of the significant features of the sample are not observable at the beginning of the measurement. Subsequent off-line processing of the listmode files allows analysis of the area of interest in a more precise manner

2.2 Target chamber setup for biomedical applications

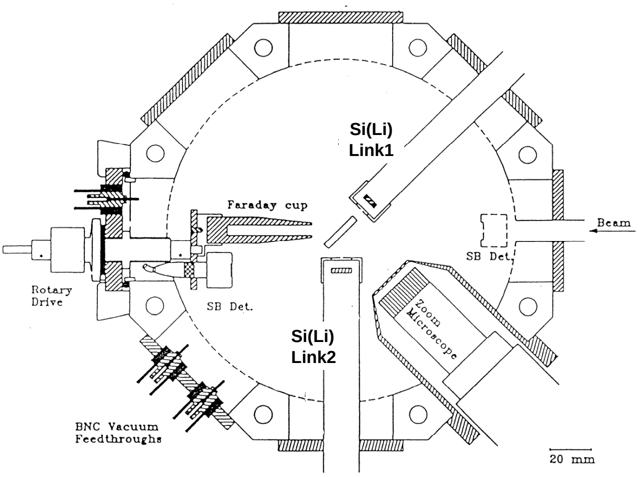

Figure 2.2: Schematic diagram of the analysis chamber

Figure 2.2 shows the schematic diagram of the analysis chamber. The chamber is of octagonal design having 8 ports defining the positions of many interchangeable components (e.g. microscope, detectors etc.). The sample is mounted on a target ladder that is inserted through a quick release opening in the XYZ manipulator accessible through the top of the chamber. Vacuum levels in the chamber are typically in the 10^{-6} mbar range which is achieved through a magnetically levitated turbo-molecular pump (SEIKO) mounted below the chamber. At these pressures, beam degradation by scattering from residual gas molecules is minimized.

A large working distance binocular zoom microscope mounted at 45^0 with respect to the beam incoming direction, is used to view the target for positioning and making the adjustments of the quadrupole excitations by using a piece of quartz to visualize the beam spot. Illumination of the target is achieved through an LED light setup mounted inside the target chamber or an external high brightness light source with a flexible mounting through a glass-covered port.

A vacuum sealed rotary shaft lead-through is fitted at the opposite position of where the beam is admitted into the chamber to facilitate the interchange of a Faraday cup and a STIM detector at the straight-through position. Therefore, the STIM detector can be positioned at any position between 0^0 to 20^0 to the beam. The Faraday cup is used to collect the charge via a vacuum feed-through to a charge integrator module (OM35e, Oxford Microbeams Ltd) with sensitivity of 10^{-14} Coulomb/pulse. Two Si(Li) detectors (Link Analytical Ltd) are mounted on both sides of the incoming beam with one at 90^0 for biomedical applications and the other at 45^0 for applications having samples mounted perpendicular to the beam direction. A surface barrier silicon detector with an active area of 50 mm^2 and an energy resolution of 12 keV is placed at a scattering angle of 160^0 for the detection of backscattered particles for RBS analysis.

2.3 Analytical techniques

An ion beam is an ensemble of particles moving in such a way that the velocity in one direction is much greater than that in other directions. The position and velocity of each particle can be specified by a point in 6-dimensional phase space (x, v_x, y, v_y, z, v_z) with the assumptions as follows [Bamf66]:

- the particles do not interact with each other
- the external forces acting on the particles are conservative (the beam is reversible)
- the velocity in z direction is much greater than that in x and y directions (i.e. the z axis is the beam direction)

These charged particles are accelerated, steered and focused using a combination of electrostatic and magnetic fields. In the non-relativistic limit, the velocity of a particle of mass A (a.m.u) and energy E (MeV) can be calculated using the following formula:

$$v = 1.389 \times 10^7 \sqrt{E/A}\ (m/s) = 0.046\, c\, (E/A)\ (m/s) \tag{2.1}$$

The radius of curvature (ϱ) of a particle of mass A, charge Q and energy E MeV traversing a magnetic field of B Tesla is:

$$B \cdot \varrho = 0.287\sqrt{EA/Q^2}\ (Tesla \cdot metre)\ \ (magnetic\ \ rigidity) \tag{2.2}$$

Then, the deflection of a beam passing through a uniform magnetic field B of length l (in Tesla.metres) is:

$$\sin\theta = 3.48B\, l/\sqrt{EA/Q^2} \tag{2.3}$$

Similarly, the deflection of a beam passing through a uniform electrostatic field $V/d(v\ m^{-1})$ of length l meters is:

$$\tan\theta = 5 \times 10^{-7} VQ\, l/dE \tag{2.4}$$

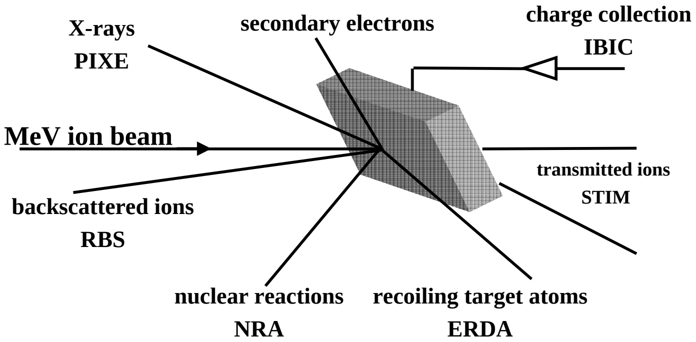

Figure 2.3: Possible interactions between a million volt nuclear particle beam and a target.

When a high energy (e.g. 2 million eV) ion beam bombards a material, many interactions occur [Zhan05]. The beam can undergo inelastic scattering with the atoms of the material, resulting in the emission of X-rays, photons and secondary electrons. It can also interact elastically with the target nuclei through Coulomb repulsion, resulting in backscattering from heavier target nuclei. Lighter atoms may also be able to recoil out of the sample.

Some possible beam-sample interactions are shown in a schematic diagram (Figure 2.3), and the associated techniques named in parenthesis. The probability of any particular process occurring depends on the energy and the identity of ion beam particles as well as the nature of the target atoms. By detecting the signals using suitable detectors, it is possible to obtain information on the elemental composition, surface structure and luminescence properties of the sample. Table 2.1 gives a list of techniques normally used in nuclear microprobe facilities.

Analytical Technique	Signal	Application	Sensitivity (ppm)
PIXE	X-rays	Elemental analysis	1-100
RBS	Backscattered ions	Stoichiometry, structure and depth profiling	1
STIM	Transmitted ions	Imaging density variation and topography	200 μg/cm^2
NRA	Nuclear reaction products	Light element depth profiling	0.01
ERDA	Recoiling ions	Light element analysis and depth profiling	2-200
IL	UV, visible and IR light	Crystal defects, rare earth and transition metals and electrical properties	0.1
IBIC	electron/hole pairs	Imaging charge collection, electrical properties and defects	N/A

Table 2.2: A list of different nuclear analytical techniques

Three of the analytical techniques in Table 2.2 are applied in the work discussed in this thesis:

- Scanning Transmission Ion Microscopy (STIM) for information on the structure and density distribution of the sample and to facilitate positioning of the unstained tissue sections prior to analysis;
- Rutherford Backscattering Spectrometry (RBS) for information on matrix composition and incident charge state;

- Proton Induced X-ray Emission (PIXE) for measuring the concentrations of elements with atomic number greater than 10. X-rays were detected using a lithium-drifted silicon X-ray detector placed at 45^0 to the beam axis and fitted with a filter designed for optimal detection of trace elements such as iron in biological specimens.

These three techniques are discussed below.

2.3.1 STIM

When the target sample is sufficiently thin so that electronic stopping dominates over the ion path of the entire thickness of the sample, the ion beam penetrates through the sample with a well defined energy loss. A solid state detector (a surface barrier detector or a silicon pin diode) can be placed behind the target for analyzing the transmitted ion energy and hence the stopping in the sample.

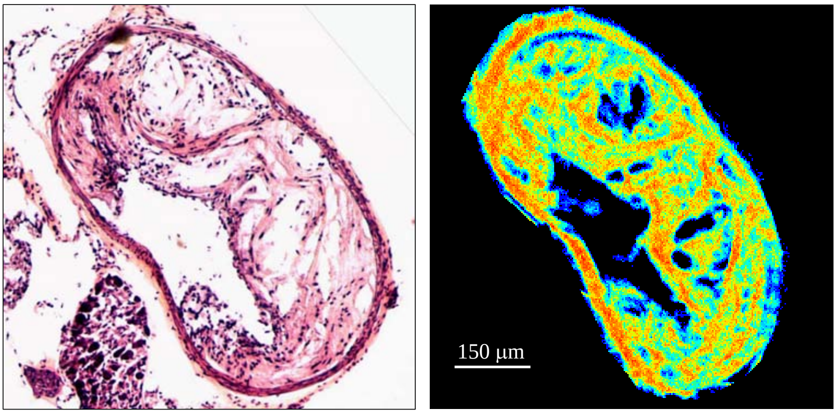

Optical image of a H&E stained section from mouse carotid artery

Off-axis STIM image of a section adjacent to the section on the left

Figure 2.4: Mouse carotid artery: optical and off-axis STIM images of a 14 μm section (Ion beam: 2.1 MeV protons).

STIM was originally investigated by Overley et al. [Over83] and Sealock et al. [Seal83] in order to obtain an area mass density image for identifying structures, which are invisible under an optical microscope.

The detection efficiency in STIM is close to 100% if the detector is placed in the beam direction (on-axis STIM). Each ion transmitted carries useful information on mass density, therefore a STIM image can be collected rapidly with a very low beam current.

STIM is used in this thesis for two purposes, firstly to assist PIXE analysis by supplying a mass density image to which the PIXE elemental images can be correlated. This can be achieved by using a surface barrier detector in an off-axis position. Secondly, high resolution STIM uses a silicon PIN diode (Hamamatsu photodiode S1223-01) as an on-axis STIM detector to study the beam damage effect and image the cells grown directly on the PIN diode with a very fine beam (down to a few tens of nm). Figure 2.4 shows the optical image of a H&E (hematoxylin and eosin: Appendix B) stained section of a mouse carotid artery (on the left) and the off-axis STIM image of a section adjacent to the section on the right and Figure 2.5 shows a high resolution on-axis STIM image of part of a cell grown on Si PIN diode.

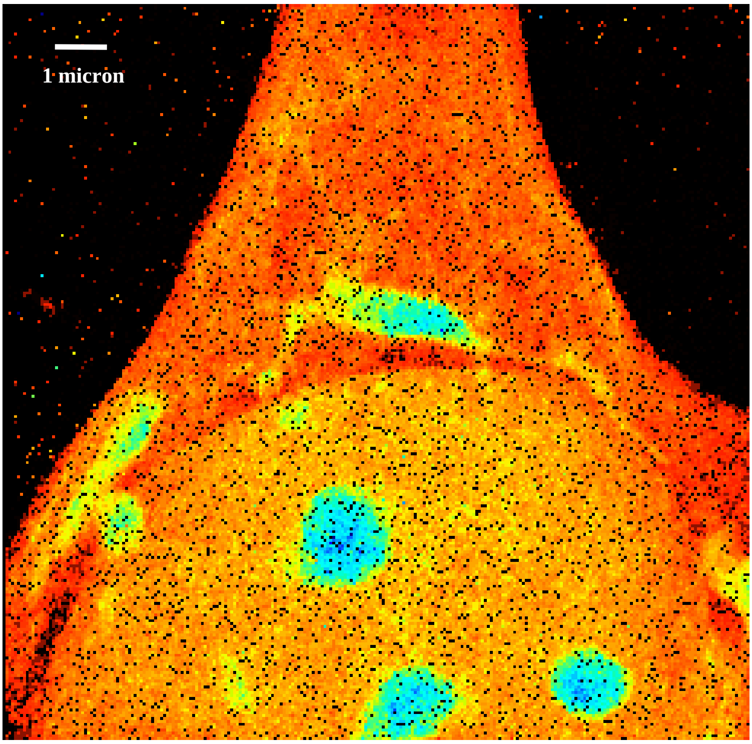

Figure 2.5: On-axis STIM image of a single cell grown on the Si PIN diode used as STIM detector (1 MeV alpha beam). The scan size is 15 μm and the STIM image has been assembled by calculating the median energy at each pixel. The beam size is 80 x 90 nm.

STIM can also be used for complementary channeling measurements. Channeling-

STIM [Bree04, Bree05] through aligning the crystal lattice to the ion beam direction can be used to characterise crystal defects using extremely low beam current, which minimizes the effects of beam damage.

2.3.2 RBS

Many years after its critical role in the discovery of the nucleus of the atom by Rutherford in Geiger and Marsden's alpha particle scattering experiment in 1911, Rutherford Backscattering Spectrometry (RBS) became a well established technique for characterizing thin films in the late 1960s.

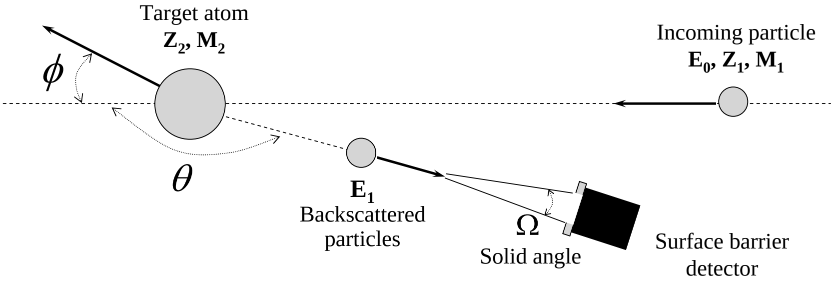

Figure 2.6: The elastic collision and typical geometry for RBS analysis.

The principle of the RBS process is shown in Figure 2.6. When an incoming charged particle with an initial energy E_0, atomic number Z_1 and mass M_1 strikes with a target nucleus (atomic number Z_2 and mass M_2) initially at rest, the two nuclei will undergo an elastic collision instead of a nuclear reaction when energy E_0 is insufficient for the projectile to overcome the Coulomb barrier. The energy of the scattered projectile, $E_1 = K_s\, E_0$, carries characteristic information about the target nuclei. The heavier the target nuclei, the less it recoils and thus the scattered particle retains most of its energy. The kinematic factor of the process can be calculated as follows [Chu78]:

$$K_s = \left[\frac{(M_2^2 - M_1^2 \sin^2\theta)^{1/2} + M_1 \cos\theta}{M_1 + M_2}\right]^2, \; M_1 < M_2 \tag{2.5}$$

where, θ is the scattering angle with respect to the incident ion direction.

The cross section σ for elastic Coulomb scattering in the center of mass frame is given by:

$$\sigma(\theta) = 1.295\,(\frac{Z_1 Z_2}{E_0})^2\,\frac{1}{sin^4(\theta/2)} \tag{2.6}$$

In the thin film approximation, the yield can be calculated after transforming equation 2.6 to the lab frame [Chu78] and when a uniform beam normally impinges on a uniform target (with N atoms/cm^3 and thickness t) larger than the area of the beam, the total number of detected particle A can be written as

$$A = \sigma \cdot \Omega \cdot Q \cdot N \cdot t \tag{2.7}$$

where, Ω is the detector solid angle, which is determined using the geometry of the detector with respect to the target ($\Omega = \frac{S_{det}}{R^2}$, S refers to the surface area of the detector and R is the distance between the detector and target) and Q is total number of incident particles. Q can be measured using a charge integrating module (OM-35e by Oxford Microbeams) via a Faraday cup.

If the cross section of the backscattering is precisely known, stoichiometry information about the sample matrix can be extracted accurately through fitting RBS spectra using a computer program SIMNRA [May97]. In our study, RBS is used to collect information on the thickness and matrix composition of the target, as well as calculating the charge.

2.3.3 PIXE

Particle Induced X-ray Emission (PIXE) is a powerful yet non-destructive elemental analysis technique, which has been used routinely in geology, biomedicine, environmental science, archaeology, art history and other fields to help answer questions of provenance, dating and authenticity since it was first introduced by SAE Johansson and his colleagues at the Lund Institute of Technology in 1970 [John70].

Quantum theory states that orbiting electrons of an atom must occupy discrete energy levels in order to be stable. Bombardment with ions of sufficient energy (usually MeV protons) will cause inner shell ionization of atoms in a specimen. Outer shell electrons then drop down to replace inner shell vacancies, however only certain transitions are allowed. X-rays of a characteristic energy of the element are thus emitted. A competing process to PIXE is Auger electron emission. In this case, the energy released in filling the k-shell vacancy are used to excite the outer shell electrons to the continuous state.

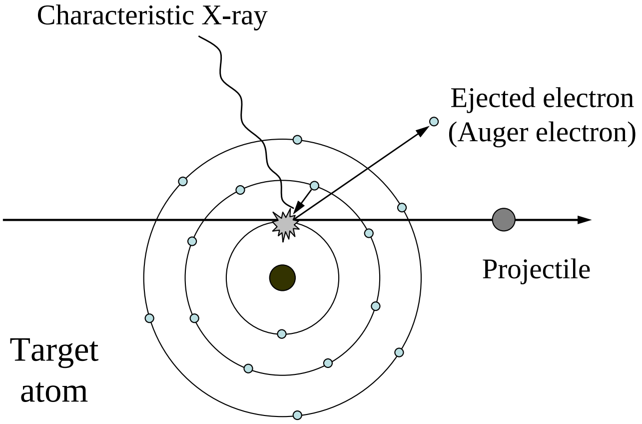

Figure 2.7: Principle of Particle Induced X-ray Emission (PIXE): a particle excites an atom, producing an electron vacancy in the K-shell and an L-shell electron de-excites and fills the vacancy in the K-shell, emitting a characteristic X-ray.

An energy dispersive detector is used to record and measure these X-rays and the intensities are then converted to elemental concentrations. The principle of PIXE is shown in Figure 2.7 and the X-ray range involved in PIXE analysis in Figure 2.8.

For a multi-element sample the PIXE spectrum consists of a number of peaks, corresponding to the characteristic K, L or M line X-rays from the elements in the sample, superimposed on a continuous background (shown in Figure 2.9). In each series (K, L etc.), the different lines are labelled by subscripts α, β and γ etc., the relative intensity of a particular X-ray line in each series is called its branching ratio. Typically, the K (transition from the L shell to the K shell) and L lines with energies below 30 keV are used for PIXE analysis. X-ray signal detection for a thin sample can be formulated as follows [John88]:

$$Y = NM \frac{\sigma \cdot \omega \cdot b \cdot \varepsilon \cdot N_{av}}{A_z} \tag{2.8}$$

where,

Y : the yield of the characteristic K_α or L_α X-ray (usually measured as the net peak area of the characteristic X-ray line)
N : the number of incident particles (usually measured as incident charge)
M : the mass area density of the atoms in question in the target (it is determined in the unit of weight per area)
σ : the ionization cross section, ω is fluofescence yield of the K or L transition
b : the fraction of of the K or L X-ray that appears in the K_α or L_α line, and
N_{av} : Avogadro's number

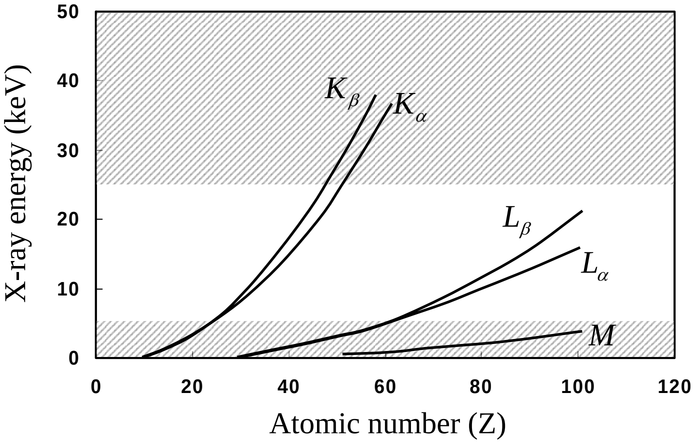

Figure 2.8: The X-ray energy of K, L and M transitions; the best working range for a Si(Li) detector is the unshaded area. After Johansson and Campbell (1988)

Equation 2.8 contains all the basic parameters needed for quantification of PIXE analysis. Sophisticated codes designed for PIXE spectrum fitting are usually employed so as to handle the data evaluation with a given level of accuracy (about 2-10%) and the quantification of element concentrations [Maxw89, Clay86].

Compared to electron based X-ray analytical techniques such as energy dispersive spectroscopy (EDS), PIXE offers better peak to noise ratios and consequently much higher trace element sensitivities as seen in Figure 2.10. This is because the background caused by bremsstrahlung of the electrons in electron-induced X-ray fluorescence is about two orders of magnitude higher than that in PIXE case. However, an accurate measurement of the detector efficiency is necessary for quantitative results.

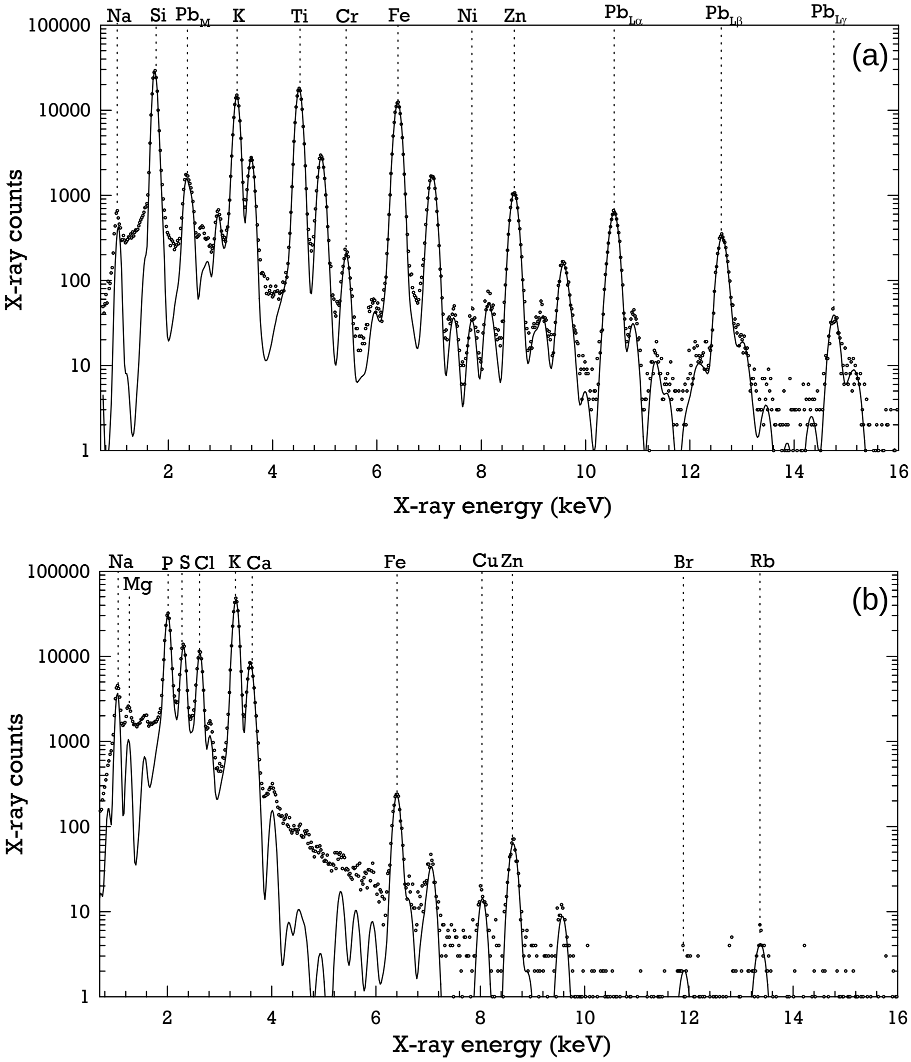

Figure 2.9: Particle Induced X-ray energy spectra of (a) the NIST standard sample of a thin glass film on Polycarbonate and (b) a 20 μm rat brain tissue. Fitted with GUPIX, Proton energy = 2.0 MeV, 300 μm perspex magic filter used in front of the Be window of the Si(Li) detector.

A typical detection efficiency curve for such detector is shown in Figure 2.11 (author's MSc thesis), for the low energy part, the limits are set by the attenuation of the X-ray intensity due to the use of vacuum sealing window (typically 12 μm Be). Ideally if an ultrathin window is used or the detector is windowless, the response range of PIXE can even go down to reach that of carbon K_α X-rays.

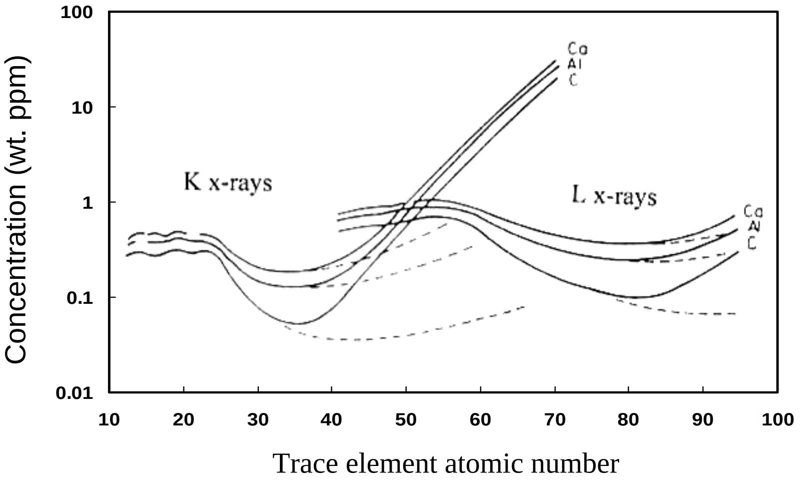

Figure 2.10: The mass detection limits of thin targets. Experimental conditions: 3 MeV protons with 100 μC charge accumulation, 1 mg/cm^2 of target thickness. After Johansson and Campbell (1988).

The mass detection limit (MDL) is closely related to the experimental conditions in terms of the following relationship [John88]:

$$MDL \propto \sqrt{\frac{FWHM}{Q\Omega}}\frac{\sqrt{\sigma_b}}{\sigma_z} \tag{2.9}$$

Where,
Q : the charge of the particle
Ω : the solid angle of the detector
σ_Z : cross-section for the X-ray peak
σ_b : cross section of the X-ray background, and
$FWHM$: energy resolution at the energy location of the X-ray peak in question.

The minimum detection limit is usually and somewhat arbitrarily defined as three times the square root of the background under the peak.

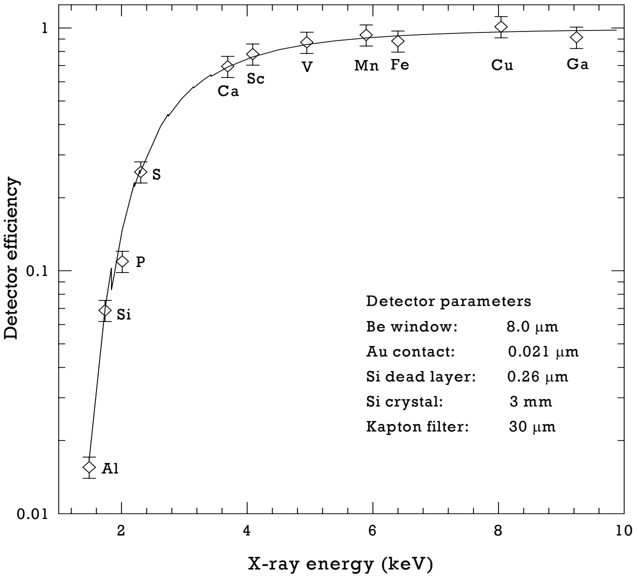

Figure 2.11: Measured efficiency of a Si(Li) detector that is used at CIBA, including transmission through a Kapton filter, versus X-ray energy in keV.

2.3.4 Image processing using BioImageXD software

In nuclear microscopy analysis, not only are the elemental concentrations important, but the imaging aspect is becoming increasingly important too. In this complementary section, the application of *BioImageXD* software that has been developed by a consortium of Finish universities, including Jyväskylä to make use of the richness of our data from the different nuclear microscopy imaging techniques is discussed in Paper 8 [Whit07].

BioImageXD software was originally developed for rendering of multidimensional Confocal Microscopy (CM) data to meet the need to render time evolution and multiple CM image channels such as different fluorescence/excitation wavelength channels in four or more dimensional hyperspace. Nuclear Microscopy presents similar visualization requirements to CM. Conventional PIXE elemental maps are on a pixel to pixel basis, which is of limited use when the concentrations of trace elements are close to minimum detection limit.

To take full advantage of subtle changes in elemental concentration correlations and the energy loss information in RBS, ERDA as well as on- and off-axis STIM image data, it is necessary to use image rendering techniques capable of handling 3- and 4-dimensional data. The list-mode data format has made possible the manipulation of available information collected during the experiments by using multidimensional visualization software tools like *ParaView* [Para01] and *ImageJ* [Rsb02] which are flexible general multi-purpose tools. In addition, *Slicer3D* [Slic03] and *BioImageXD* [Bioi04] are directed towards rendering X-ray and magnetic resonance tomographic images.

In this work, we have explored the applicability of software packages *ImageJ* and *BioImageXD* for multidimensional biological image analysis, processing and multidimensional rendering for visualization in nuclear microscopy. These two software packages in particular deal with microscopy image rendering, they are chosen because they are available in the public domain for a wide range of common computer platforms.

Using *ImageJ*, the co-localization of elements in elemental maps can be done quantitatively based on its ability of assigning different colors to different elements. Colocalisation of the Ca and P signals is shown in Figure 2.12 a & b (these images can be compared with the images in Figure 1.1). The white color channel denotes areas where the Ca and P is strongly colocalised that could be indicative of calcium phosphate deposits [Watt06]. This technique can also be set to only render colocalised elements where the elemental composition ratio corresponds to particular chemical compounds that cannot be uniquely identified using Nuclear Microscopy technique because the use of characteristic X-rays are not sensitive to chemical structure.

Figure 2.12 c & d present a cultured breast cancer cell grown from MCF7 cell-line (please refer to chapter 6 for more details) imaged using a 1 MeV alpha beam. These images have undergone 3D surface and volume rendering in different ways using *BioImageXD*. For example, Figure 2.12d presents a 4-dimensional representation of the energy loss distribution as Figure 2.12c. By assigning these levels different colors and observing the image during slow rotation to enhance the sensation of vertical depth in the image, it was found that the "noise" was a hidden structure in the energy loss distribution along the z direction. Such structure is not apparent when using the average energy loss for the representation (Figure 2.12c). The detailed interpretation of the references in color in Figure 2.12 can be found in paper 8.

Focused MeV ion beams are not restricted to obtaining microscopic images; they can be also used to write microscopic structures. This is known as MeV ion beam writing, or (as is common) if protons are used, proton beam writing. The low beam current requirements mean that the beam can be more tightly focused than for Nuclear

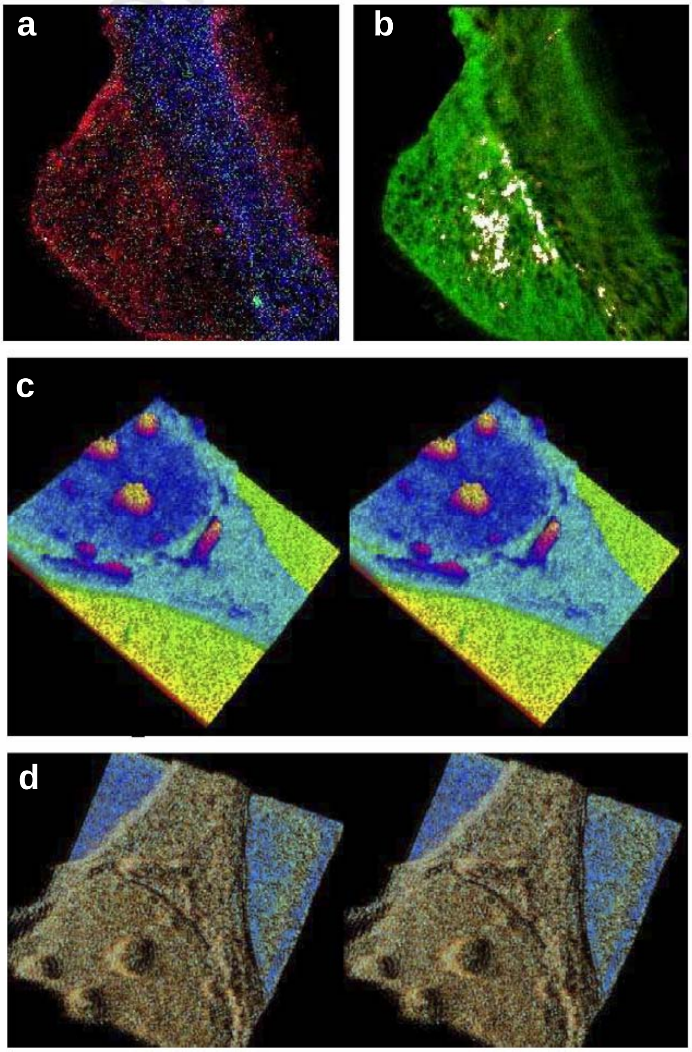

Figure 2.12: (a,b): Colocalisation of PIXE maps using *ImageJ* from PIXE elemental maps of a rabbit aorta arch [Watt05], the luminosity of each color channel has been expanded to optimize the visibility of correlations. (c): Free vision parallel stereo pair of Warp-scalar representation the average energy loss map using *BioImageXD* with smoothing, (d): Free vision parallel stereo pair representation of the data represented by (x, y, z, color + luminance) where z corresponds to ΔE, and color + luminance corresponds to yield (paper 8).

Microscopy. A brief introduction is given below because the lithography system was used in some of the experiments carried out in this thesis and the technology is similar to Nuclear Microscopy.

2.4 Modification technique - Proton beam writing

There are currently three modification techniques which are based on ion beam processes capable of fabricating structures at the sub-100 nm level. They are: 1) the focused ion beam (FIB) technique where a slow focused heavy ion beam (energy around 30 keV) is written over a surface to create a pattern through modification, deposition or sputtering; 2) proton beam writing, in which fast (typically MeV) protons are used to direct-write deep precise 3D patterns into resist. The relatively high energy of the incident protons produce high penetration into the resist (eg a 2 MeV proton will penetrate 60 μm into PMMA); and 3) ion projection lithography (IPL), where medium energy ions (typically 100 keV) are projected through a patterned mask for rapid fabrication. A special variant of the latter technique that combines proton beam writing with ion projection lithography is used in Jyväskylä [Gore07].

All these three techniques have highly appropriate and complementary application areas. However, PBW is the only technique which offers the capability of direct-write high aspect ratio nano- and microstructures. This technique, pioneered at the Center for Ion Beam Applications (CIBA), National University of Singapore, has the unique ability to direct write precise high-aspect-ratio 3D nano-patterns in conventional resists such as PMMA (positive resist) and SU8 (negative resist). When the resist is developed, material removal rates of around 10^6 μm^3 per nC of incident protons can be realized, making the process up to one million times more efficient than conventional FIB for 3D patterning [Watt05]. Work carried out using the proton beam writing technique in CIBA has shown that p-beam writing is very effective in fabricating high aspect ratio and multi-level structures (shown in Figure 2.13) [VanK03, VanK04].

The P-beam writing technique has been used for studies related to tissue engineering. The idea is to produce precise 3D microgrooved structures and micro-patterns to study the relation to topographic guidance of cells. Tailor made 3D micro-structures might be useful when multiple cell types are needed to form proper tissue in cases where fibroblast overgrowth is detrimental to the formation and function of the tissue [Sun04].

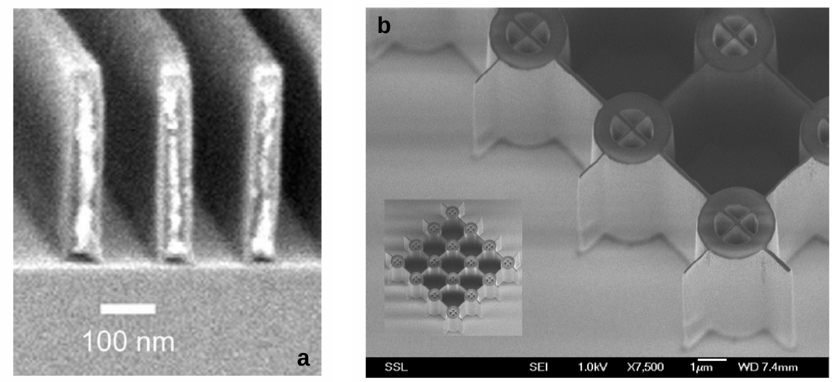

Figure 2.13: Well defined structures by using p-beam writing technique: (a) 50 nm walls fabricated in PMMA using p-beam writing with 2 MeV protons, (b) high-aspect-ratio structures fabricated using p-beam writing with 1 MeV protons in SU8 negative resist, showing 60 nm wall 10 μm deep structures [VanK03, VanK04].

2.5 Figures of merit for beam focusing

The research work in this thesis and the emerging proton beam writing technology largely depends on a focused ion beam. The best results for focusing proton and alpha beams with MeV energies to nanometer sized beam spots have been obtained using quadruple triplet lens systems [VanK04]. These lens system produces a demagnified image of a precision aperture with different horizontal and vertical demagnification, D_x and D_y. The quadruple elements are connected so that achieving optimum focus requires simultaneous optimization of two currents.

In paper 9, we present a study on developing a procedure to yield separate figures of merit (FOM) in the horizontal and vertical directions. The procedure is based on measurement of central peak of the 2D autocorrelation function (ACF) [Lynn73] of an image. It is expected to provide a real time indication of focus quality for manual (and passive automatic) focusing [Udal05] in proton beam lithography and imaging with quadrupole multiplet lens systems. The figure of merit has the important advantage for ion beam imaging of biomedical samples in that the fluence needed is considerably lower than for edge fitting, which is normally done to determine the exact size of the beam spot achieved for a particular experiment.

The experimental tests were carried out using the proton beam writing facility in the Center for Ion Beam Applications (CIBA). The focusing Ni grid used for this work was fabricated by p-beam writing technique in CIBA and subsequently electro-depositing Ni in a plating bath before detachment [VanK04] and this grid was mounted on a computer controlled precision X-Y-Z stage [Watt03]. The proton induced secondary electron yield was used to image the sample. Coarse focusing of the beam was carried out by optical inspection of the beam spot fluorescence on a quartz target and subsequently, in order to obtain a focus condition very close to the optimal, the edge sharpness was monitored as the beam was scanned in lines across the grid bar edges in both horizontal and vertical directions. Serial images were acquired where the horizontal and vertical lens currents were varied in steps through focus. The autocorrelation function was calculated using a Wiener-Khinchin approach where Fourier transforms were calculated using the *FFTPACK5* software package [Fftp05]

This method allows simple filtering to minimize the effects of pixel to pixel statistical noise and makes no assumption as to the structure of the sample. The rms widths of the ACF correctly reproduced the optimum focus condition and the behavior under defocusing conditions of the FWHM beam profile that was determined from the same data by non-linear fitting. Evaluation of the figure of merit takes less than a second using a modern processor which is sufficiently fast to allow the figures of merit to be used directly for manual focusing and automatic focus control.

2.6 Closing remarks and outlook

Nuclear Microscopy is ideal for studies including bio-mineralization, metal uptake by plants and micro-organisms, metabolism of metals and its dysfunction and metals and environmental exposure. The improvement of spatial resolution will enable the observation of sub-cellular components directly. Vertical geometry microbeam facilities are being developed to allow samples to be kept in liquid culture media using external beam measurement techniques.

3 Resolving power of focused MeV ion beam methods for bio-materials

In using Nuclear Microscopy methods for practical applications in biomedicine, important issues are: i) how good a resolving power can be achieved; ii) what the processes are that limit the biomedical applications; and iii) how these might be optimized. This chapter deals with how the thickness of the biological sample interferes with the attainable spatial resolution.

3.1 Focusing and angular spreading contributions

The process of focusing the MeV ions into a 1 μm or smaller diameter probe involves many technical aspects. A prime example of this is the lens used to focus the ion beam, which is a fourfold symmetric quadrupole lens, with a pole shape that is difficult to manufacture to a sufficient degree of precision. The lens system, which is made up of multiple quadrupole lenses, can suffer mechanical defects, large aberrations etc, which prevent the achievement of a 1 μm (or smaller) probe. The depth of field is another factor that limits the resolution as the target becomes thicker.

The large number of collisions of the MeV ions in the sample result in energy straggling, and lateral spread of the beam in the sample. These effects are intrinsic effects because they are independent of the instrument and these effects limit the depth and lateral resolution attainable with MeV ion beam analytical and imaging techniques. They originate from the statistical nature of the ion-sample interaction and not the instrument used. The mass and depth resolution attainable with backscattering spectrometry, the minimum resolvable areal density with STIM and the depth resolution with RBS and NRA are limited by the energy straggling.

The lateral beam spreading, rather than the beam spot size on the target surface, ultimately defines the minimum spatial resolution attainable with the nuclear microprobe in thick layers. However, it turns out that a spatial resolution of approximately 100 nm can be maintained for several microns through the sample. The lateral spread of a MeV ion beam is considerably less than that for keV electrons.

In this chapter, we will be investigating the contribution of the angular and lateral spread of the beam in biological specimen to the spatial resolution of a microbeam.

3.2 Angular and lateral spread of light ions penetrating bio-materials

When an initially well collimated ion beam traverses through a target, nuclear elastic scattering gives rise to a lateral spread of the beam, and this scattering increases the width of the beam profile. It plays an important role in a number of fields such as ion beam analysis (IBA), ion implantation, ion beam lithography, particle detection, beam transport in accelerators, fusion research and ion beam therapy.

The trajectory of MeV ions in matter is usually approximated by straight lines. This is, however, only a crude approximation due to many small angle deflections by collisions with large impact parameters (multiple scattering). The combined effects of these collisions result in angular and energy straggling, leading to degradation of the achievable depth resolution. A clear understanding of these angular distributions is of prime importance in nuclear microanalysis in which multiple scattering is an effect limiting the experimental resolution.

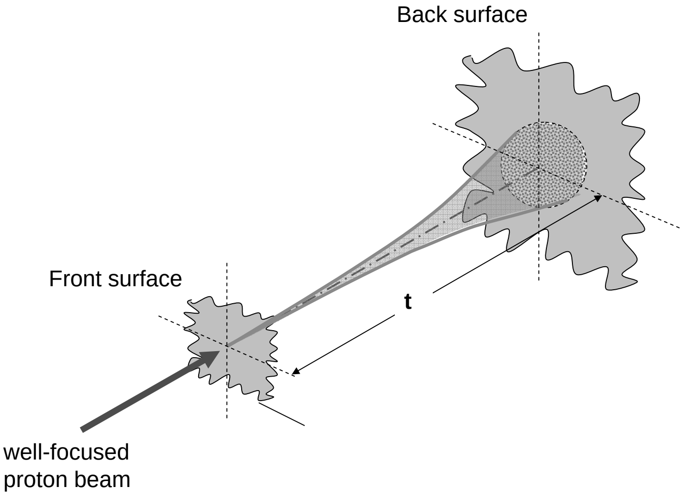

Figure 3.1: Schematic drawing of how a well-defined ion beam spreads because of multiple scattering after traversing a depth of t in a biological sample.

Early theoretical work on small angle multiple scattering of ions has been carried out since the 1920s by pioneers such as [Both21, Moli48, Meye71]. Scott [Scot63] summarized the state of knowledge in this field in 1963. A seminal contribution was brought in by Sigmund and coworkers in a series of papers [Sig74, Marw75, Sig78], including tabulated spatial angular distributions widely used since then in the experimental field.

Presented in this chapter is a study of how small angle multiple scattering of MeV light ions (2.1 MeV Protons) limit the spatial resolution of nuclear microscopy for biological samples (in particular, smooth muscle cells arterial wall) (shown in Figure 3.1). Two approaches were investigated: an analytical approach which gives important information about how the spreading of the ion beam scales with thickness and target atomic number and a computational approach which gives more accurate answers - but is less suitable for scaling purposes.

3.2.1 Basic analytical theory of multiple scattering

When traveling along a path x through matter, an energetic ion will continuously lose energy due to the interaction with electrons and screened nuclei. The energy loss per unit path-length is denoted as *stopping force* [1].

$$B = -\frac{dE}{dx} \tag{3.1}$$

Often, the stopping is normalised to the atomic density N of the substance, resulting in the *stopping cross section*:

$$S = -\frac{1}{N}\frac{dE}{dx} \tag{3.2}$$

where $N \cdot x$ is the number of atoms per unit area for a traversed path-length x.

The stopping force dE/dx is determined by Coulomb interactions with the substrate atoms and electrons,

1. Nuclear collisions, in which energy is transferred from the ion to the target nuclei (called nuclear stopping or elastic energy loss);

---

[1] The more modern terminology "stopping force" is used for dE/dx (distance differential of energy) rather than "stopping power" because "power" implies the time differential of energy, dE/dt.

2. Electronic collisions, in which the moving particle collides with, excites or ejects atomic electrons, and energy is transferred from the ion to target electrons (called electronic stopping or inelastic energy loss).

The relative importance of the various interaction processes between the ion and the target medium depends on the ion velocity and the charges of the ion and target atoms. The stopping force describes the mean energy loss. In addition, the energy distribution of an ion beam is broadened after traversing a thin sheet of matter through multiple scattering process.

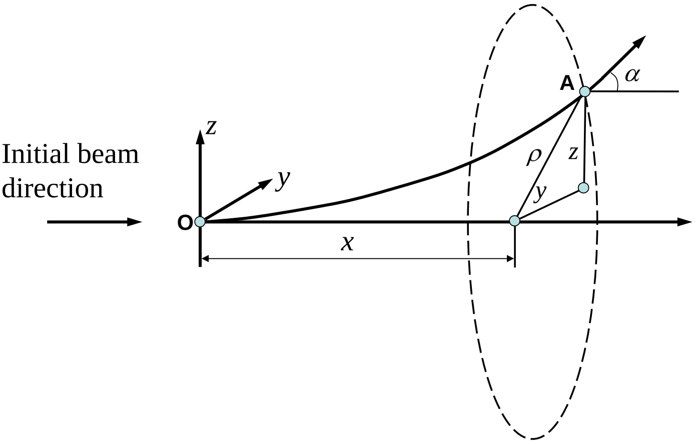

Figure 3.2: The initial beam direction is along the positive x direction the x-axis. We consider a lateral displacement: ($\rho = \sqrt{y^2 + z^2}$), and angular deviation α after a penetrated depth x. The dashed line outlines the plane of the beam profile with a circular distribution (radius: ρ) after traversing a thickness of x (after Marwick and Sigmund [Marw75]).

For MeV light ions, multiple scattering is essentially due to small angle elastic collisions with the target atoms. The general picture is simply that with each collision with a target atom, the ion loses energy and at the same time changes direction (shown in Figure 3.2). The trajectories of fast charged ions in matter, of 0.1-100 MeV proton or helium ions, are mainly determined by successive inelastic and elastic binary encounters with the atoms of the medium, resulting in energy loss and angular multiple scattering.

The statistical nature of the nuclear collisions leads to a broadening of the angular distribution of an ion beam, as indicated in Figure 3.3a. When traversing through a slab of matter with thickness x. The angular distribution of the ions depends on the depth and can be described by a distribution function $f_\Omega(x,\ \alpha)$, with the normalization condition [Anne88]:

$$1 = \int f_\Omega(x,\ \alpha)\, d\Omega = 2\pi \int_0^\pi f_\Omega(x,\ \alpha)\, \sin\alpha d\alpha \approx 2\pi \int_0^\pi f_\Omega(x,\ \alpha)\, \alpha\, d\alpha \qquad (3.3)$$

where the latter equality holds for small angles. More precisely, $f_\Omega(x,\ \alpha)$ represent the distribution over the solid angle. Alternatively, the polar angle distribution $f_\alpha(x,\ \alpha)$ can be employed with the normalization:

$$1 = \int_0^\pi f_\alpha(x,\ \alpha)\, d\alpha \qquad (3.4)$$

Comparing the equations (3.3) and (3.4) above, both distribution functions can be transformed into each other (for small angles) by the following equation:

$$f_\alpha(x,\ \alpha) = 2\pi\alpha f_\Omega(x,\ \alpha) \qquad (3.5)$$

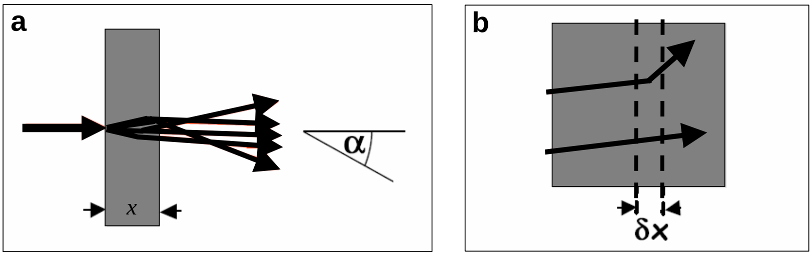

Figure 3.3: (a) Multiple scattering of an ion beam, (b) "Forward" transport by nuclear collision.

In order to study the evolution of the distribution function at increasing penetration depth, we assume a thin incremental slab δx shown in Figure 3.3b, which describes an example of so-called *forward* transport. Within this slab, each ion can either change its direction due to a nuclear collision, or it may just penetrate through without any nuclear collision (any energy losses are neglected). In the former case, for an ensemble of ions described by the angular distribution function, the new distribution function, $f_\Omega(x+\delta x,\ \alpha)$ results from scattering events which transform fractions of the original function, $f_\Omega(x,\ \alpha')$, into the direction α. The probability is given by the scattering cross sections for all directional changes $\alpha' \rightarrow \alpha$. In the latter case, the distribution function is reproduced with a probability of one minus the total cross section. Therefore:

$$f_\Omega(x+\delta x,\ \alpha) = n\delta x \int d\sigma_n(\alpha' \rightarrow \alpha) f_\Omega(x,\ \alpha') + (1 - n\delta x \int d\sigma_n) f_\Omega(x,\ \alpha) \tag{3.6}$$

The Taylor expansion of the left-hand side results in a *Boltzmann* type of transport equation:

$$\frac{\partial f_\Omega(x,\ \alpha)}{\partial x} = n \int d\sigma_n(\alpha' \rightarrow \alpha)(f_\Omega(x,\ \alpha') - f_\Omega(x,\ \alpha)) \tag{3.7}$$

By suitable mathematical techniques, the integro-differential equation (eq. 3.7) can be solved for an initially sharp angular distribution, $f(0,\ \alpha) = \delta(\alpha)$, in the Bothe equation (where J_0 denotes the zero-order Bessel function):

$$f_\Omega(x,\ \alpha) = \frac{1}{2\pi} \int_0^\infty k dk J_0(k\alpha) exp(-n\sigma_0(k)) \tag{3.8}$$

with

$$\sigma_0(k) = \int_0^\infty \frac{d\sigma_n}{d\Theta} d\Theta (1 - J_0(k\Theta)) \tag{3.9}$$

where, by following the usual notation [Sig74, Lind63], the differential scattering cross section $d\sigma$, for incident ions with mass M_1 and atomic number Z_1, in a target characterized by the atomic number Z_2 and mass M_2, can be cast in the form:

$$d\sigma = -\frac{\pi a^2}{2} t^{-3/2} f(t^{1/2}) dt \tag{3.10}$$

where:
$t = \varepsilon^2 T/T_m$,
$T_m = \gamma E$, (maximum energy transferred)
E is the initial energy of incoming ion,
T is the recoil energy, $0 \leq T \leq T_m$,
$\gamma = 4M_1M_2/(M_1+M_2)^2$,

M_1 is the mass of scattered particle,
M_2 is the mass of recoil particle,
Z_1 is the atomic number of scattered particle,
Z_2 is the atomic number of recoil particle,
a is the Thomas-Fermi screening radius.

$f(\mathrm{t}^{1/2})$ is a function that depends on the assumed form of the screening function. The screening function describes how the nuclear change is shielded by orbiting electrons. t the reduced energy-angle variable (also referred to magic "t"), Following Sigmund [Sig74], the Bothe equation can be transformed into ***reduced units***. The (small) laboratory scattering angle θ can be related to the reduced scattering angle by:

$$t^{1/2} = \varepsilon \sin\frac{\theta}{2} \approx \frac{1}{2}\varepsilon\,\theta \quad (\varepsilon = \frac{aEM_2}{Z_1Z_2e^2(M_1+M_2)}) \tag{3.11}$$

where "a" is Thomas Fermi screening radius, correspondingly, the directional angle can be transformed into a reduced angle:

$$\tilde{\alpha} = \frac{aE}{2Z_1Z_2e^2}\,\alpha \tag{3.12}$$

Further, a reduced thickness τ is introduced for the purpose of multiple scattering:

$$\tau = \pi a^2 Nx = \frac{6.895 \times 10^{-17} Nx}{(Z_1^{1/2} + Z_2^{1/2})^{4/3}} \tag{3.13}$$

here the Firsov screening length ($a = 0.8853 a_0/(Z_1^{1/2}+Z_2^{1/2})^{2/3}$), with the Bohr radius: $a_0 = \hbar^2/m_e e^2 = 0.0529\ nm$ is used for a two atom system, N is the atomic density (atoms/cm^3), x thickness (cm). Then equations (3.8) and (3.9) can then be expressed in the reduced units as follows:

$$f_{\tilde{\Omega}}(\tau, \tilde{\alpha}) = \frac{1}{2\pi}\int_0^\infty z dz J_0(z\tilde{\alpha}) exp(-\tau\triangle(z)) \tag{3.14}$$

with

$$\triangle(z) = \int_0^\infty d\tilde{\varphi}\frac{f(\tilde{\varphi})}{\tilde{\varphi}^2}(1 - J_0(z\tilde{\varphi})) \tag{3.15}$$

Multiple scattering distribution functions have been tabulated for a large range of reduced angles and thickness in Refs [Sig74, Anne88], and based on this data, Bird et al [Bird89] fitted a simple functional form which related the reduced half angle $\tilde{\alpha}$ to reduced thickness τ with the parameters listed in Table 3.1:

$$\tilde{\alpha}_{1/2} = k\ \tau^{p} \tag{3.16}$$

τ	k	p
3 - 20	0.3617	0.7237
30 - 200	0.4865	0.6285
100 - 2000	0.5899	0.5894
10^3 - 10^6	1.0	0.55

Table 3.1: Parameters for equation (3.15)

For our case and for most applications, the first set of parameters is adequate: the fit obtained deviates less than 2%, 5% and 12% for τ values up to 20, 40 and 80 respectively. Then the ***real half angle*** $\alpha_{1/2}$ can be obtained from the ***reduced half angle*** $\tilde{\alpha}_{1/2}$ found using the above mentioned method via formula:

$$\alpha_{1/2} = \frac{2Z_1Z_2e^2}{aE_1}\ \tilde{\alpha}_{1/2} \tag{3.17}$$

E_1 (keV) is the average energy deposited in the range x the ion particles traversed.

The lateral spread was found to be related to the angular spread via the relation [Sig74]:

$$\rho_{1/2} = x\ \alpha_{1/2}\ \Gamma \tag{3.18}$$

where Γ is the lateral spread scaling function given by Marwick and Sigmund [Marw75] and plotted in Figure 3.4. This function varies slowly at large values of τ and maybe approximated by $\Gamma = 0.8$. The formula below can be used for more accurate calculations:

$$\Gamma = 1.77 + 0.172\ \tau^{-0.335} \tag{3.19}$$

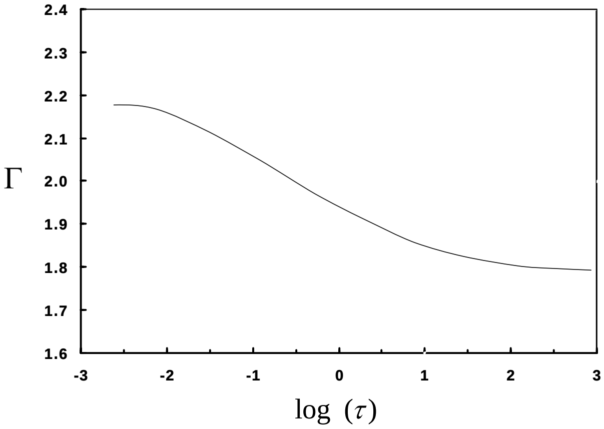

Figure 3.4: The lateral spread scaling function Γ as a function of reduced thickness τ, equation (3.18) after Marwick et al [Marw75].

3.2.2 Monte Carlo computational approach - SRIM

SRIM (The Stopping and Range of Ions in Solids) [Zieg85] is a set of programs which calculate the stopping and range of ions into matter using a non-quantum mechanical treatment of ion-nucleus collisions and a pseudo-empirical quantum mechanical treatment of ion-electron collisions. In this treatment, a moving atom is assumed to be an 'ion', and all target atoms as 'atoms'. The statistical algorithms used in the programs for calculation allow the ion to make jumps between the calculated collisions and correct for the electronic stopping over the intervening step. The ion and atom are considered during the collisions to have a screened Coulomb interaction including exchange and correlation interactions between the overlapping electron shells.

The possibility of tailoring the statistical probability of the ion encountering a particular element according to the stoichiometry means compound targets can be handled. It is stressed that such Monte Carlo codes should not be used uncritically. In our case we have considered important issues such as the cut-off that selects the smallest angle collisions that can contribute to the angular distribution, and ensure the target is sufficiently thick compared to the mean free distance between collisions.

Biological samples by nature are multi-elemental, and we have to use average atomic number and average atomic weight for our calculation while in SRIM program, Ziegler, Biersack and Littmark have performed potential calculations for a wide range of particle pairs (522 atoms pairs). They assumed solid state charge distributions for both particles, which were constructed by using a Hartree-Fock-Slater [Froe77] method or in some cases by local density approximations for exchange and correlation effects.

3.2.3 Calculation of 2.1 MeV protons in biological samples - analytical and SRIM results

Here we use the results from the previous section for the calculations of fast light ions in biological samples.

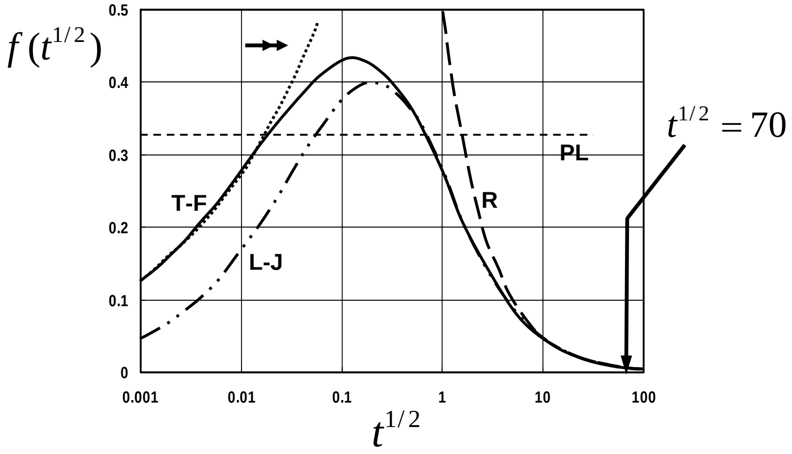

Figure 3.5: Universal scattering function according to Lindhard, Nielsen, and Scharff, as function of the reduced scattering angle for pure Rutherford scattering (R), Thomas-Fermi (T-F), Lenz-Jensen (L-J), and power-law (PL; s=2, k_s=0.8) screening, and a low- t approximation to T-F screening according to formula: ($f(t^{1/2}) = 1.43 \times (t^{1/2})^{0.35}$) (double arrows).

The scattering function $f(t^{1/2})$ in equation (3.10) is a function that depends on the assumed form of the screening function and can be determined (e.g. by numerical integration) from the approximate interatomic potential [Lind63]. When only a limited range of $t^{1/2}$ value is considered, the interatomic potential can be approximated by a power law potential: $V(r) \propto r^{-1/m}$. Then the Lindhard scattering function $f(t^{1/2})$ can be written as [Wint70]:

$$f(t^{1/2}) = \frac{\lambda' t^{1/6}}{[1 + (2\lambda' t^{2/3})^{2/3}]^{3/2}} \tag{3.20}$$

For 2.1 MeV protons (Z_1=1, M_1=1) in biological samples (in our case: arterial wall with an elemental composition of $\mathrm{C}_{0.4}H_{0.08}O_{0.12}N_{0.4}$, gives an average atomic number Z_2 of 6.225 and an average mass M_2 of 12.37), the reduced scattering angle t is calculated to be greater than 4900 according to equation (3.11) using Firsov screening length.

According to the graph shown in Figure 3.5, for the reduced scattering angle $t^{1/2} \geq 70$, the scattering function for many models converge towards the pure Rutherford scattering cross section region where the ion velocity is large enough to fully penetrate the inner-most atomic electron shells, the interaction can then be treated as a pure Coulomb interaction. In this case, the interatomic potential we choose to use should not give very different results from the SRIM calculations. Although the approach used in SRIM by Ziegler et al has been considered somewhat superior to the Firsov, Lindhard and Bohr approaches, the difference is only obvious for lower projectile energies.

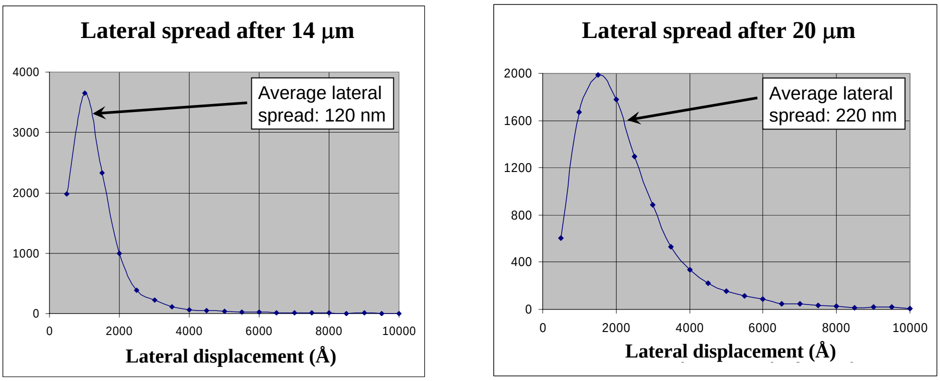
Lateral spread after 14 µm

Lateral spread after 20 µm

90% of the ions lie within 200nm

87% of the ions lie within 350nm

Figure 3.6: Histogram of 10,000 ions through 14 μm and 20 μm (SRIM simulation).

For high energy light ions, electronic energy loss dominates the stopping force on point charges by more than three orders of magnitude and so we have good reason to ignore the nuclear stopping. In our particular case, the electronic stopping is calculated to be more than 70,000 times of the nuclear stopping. It is evident that nuclear stopping is negligible except for its contribution to multiple scattering and electronic stopping which dominates in this case.

Based on the small angle multiple scattering theory described so far and the formulae derived from the analytical theory, we have made a calculation of the *reduced half angle* ($\tilde{\alpha}_{1/2}$), *half angle* ($\alpha_{1/2}$) and *lateral spread* (ρ) for sample thickness from 1 μm to 20 μm of biological tissues (the maximum tissue section thickness we have experimented with so far is 20 μm). SRIM simulation of 10,000 ions traversing the same range of sample thicknesses has also been performed.

Figure 3.6 shows two histogram graphs from SRIM calculations of 10,000 ions traversing through 14 μm and 20 μm dry tissue. The calculation shows that about 90% ions still lie within a radius of 200 nm after having traversed a thickness of 14 μm tissue and 87.4% ions still remain within a radius of 350 nm after a piece of dry tissue with a thickness of 20 μm. The average lateral spread of the 10,000 ions is calculated to be 120 nm and 220 nm in 14 μm and 20 μm tissue respectively. The fall-off towards zero lateral displacement seen in these figures is a consequence of few collisions, the area normalization and the low impact parameter cut-off [Winz00] used in the binary collision approximation SRIM code [Zieg85]. Detailed discussion is outside the scope of this thesis and the only comment made is that the normalisation implies the fall off has only a small influence on the width of the distribution.

In order to span a wide range of reduced thickness τ, a piecewise approach with the values of k and p in equ. 3.16 given in Table 3.1 was used. In order to test the sensitivity to details of the ion screening, two different screening lengths (Lindhard and Firsov) were used. The results of these calculations are compared with SRIM results in Figure 3.7.

It can be seen that the analytical results are close to the results using SRIM. In conclusion, even though the Sigmund-Marwick-Winterbon [Sig74, Marw75] formalism used in our calculation for angular and lateral spread gives better insight to the underlying physics (e.g. cross section, flux distribution, etc...); in addition it does not introduce a low impact parameter cut off, its application is limited because:

- It is restricted to simple analytical potentials;
- It is difficult to apply to multi-elements targets (average atomic mass and number approach needed, giving large uncertainties);
- It yields the distribution halfwidths directly;
- It assumes an an amorphous homogeneous target of a single element (not realistic for biological materials).

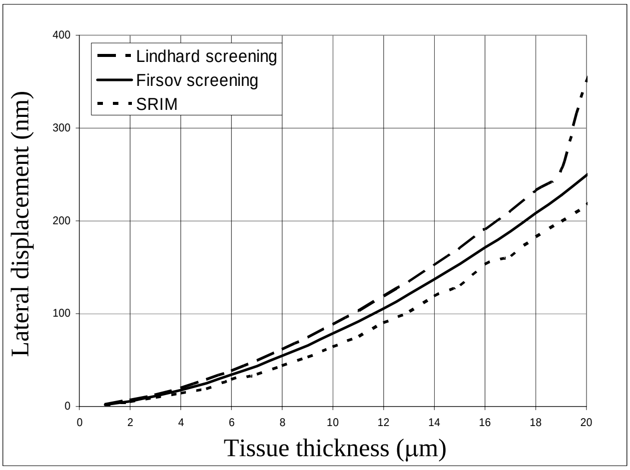

Figure 3.7: Calculation results showing the lateral spread in nanometers (y axis) as function of tissue thickness in micrometers (x-axis) traversed by the projectile ions (2.1 MeV protons).

The results obtained are consistent with the results from the Monte Carlo calculation using SRIM, which is more user friendly but scaling etc. is more intractable.

3.3 Comparison with beam divergence from the focusing system

The beam divergence is the increase in beam diameter with distance from the aperture from which the beam emerges in any plane that intersects the beam axis. An ion beam that has been focused on to the surface of a biological sample by a probe-forming lens system of a nuclear microprobe can have a relatively steep convergence angle, determined by the brightness of the ion source of the accelerator, the slits settings and the demagnification factor of the probe forming lens system and the minimum beam current required to obtain statistically significant data in a reasonable time without damaging the sample excessively.

Figure 3.8 illustrates schematically how a focused ion beam is projected onto a sample by a focusing lens system with a given demagnification factor. x is the distance between the object slits and collimating slits. x' is the distance between collimating slits and sample. α is the divergence angle and α' is the convergence angle. The origin of the contribution to broadening from the beam convergence and divergence about the focus plane is illustrated in 3.9.

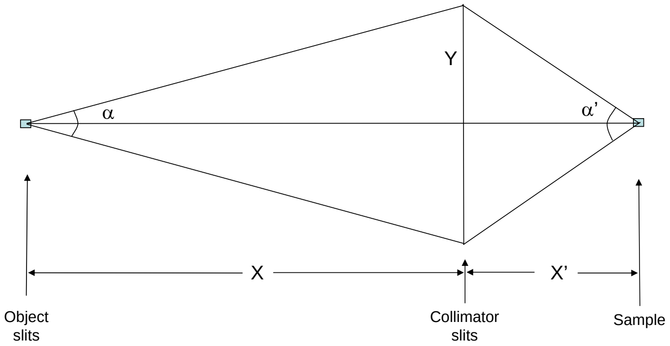

Figure 3.8: Schematic diagram showing how the beam diverges, converges and transported between object slits, focusing lenses, collimator slits and sample.

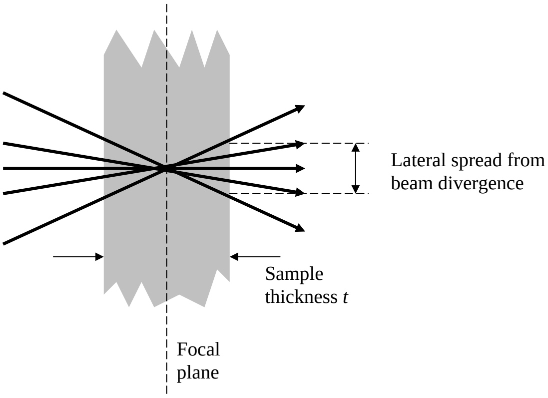

Figure 3.9: A schematic diagram illustrating the contribution of convergence and divergence to beam broadening.

The projects in this thesis were carried out using mainly the CIBA 10^o and 30^o beam lines. The data for the two systems are given in Table 2.1. In the case of the Nuclear Microscopy system, the beam divergence (half angle) is $0.00045^o \times 0.0013^o$ for a typical collimating aperture size of 50 × 150 μm while the lithography system it is $0.00001^o \times 0.00036^o$ for a typical collimating aperture size of 10 × 40 μm (shown in Table 3.2).

	Nuclear Microscopy line	P-Beam Writing line
Beam line	30^o	10^o
x	6.4 *m*	6.4 *m*
x'	16 *cm*	7 *cm*
D_x	88	228
D_y	24	60
Collimator slit size	50 × 150 μm	10 × 40 μm
α	$0.00045^o \times 0.0013^o$	$0.00009^o \times 0.00036^o$
α'	$0.0396^o \times 0.0322^o$	$0.0205^o \times 0.0216^o$

Table 3.2: Divergence parameters for the nuclear microscopy beam line and p-beam writing beam line (assuming the beam is a point at object slits).

The spreading of the beam spot size for a depth of focus corresponding to the worse case film thickness of 20 μm is 140 x 110 nm and 72 x 75 nm for the nuclear microscopy and proton beam writing beamlines, respectively.

3.4 Conclusions

From the results presented in this chapter, for typical dry tissue section thicknesses of less than 20 μm, the resolution is dominated by the lateral spreading of 2.1 MeV protons in the sample. This is less than 350 nm in radius (about 0.5 μm FWHM after integration and averaging). However, it should be borne in mind this is the worst case, because of the energy dependence of X-ray production cross section and X-ray absorption limits the sensitive depth to a layer just close to the surface.

The analytical model is limited because of the need to assume an average atomic number and mass. This is particularly unsatisfactory for biomaterials because it's really difficult in many cases to specify the elemental composition. SRIM is considered to be more realistic because it treats the different target elements separately. However, predicting the distribution in the small angle limit can be problematic. The semi-empirical analytical model is useful for predicting the thickness and shape scaling effects even if the absolute values are not as accurate as the Monte Carlo model that forms the basis of SRIM. The semi-empirical model might be improved by treating the target as being made up with thin layers of constituent elements rather than atoms of aggregate atomic number and mass.

The contribution to the beam divergence is small compared to the contribution from multiple scattering in the sample film for the focused ion beams used in this work.

4 Iron, zinc and induced atherosclerosis in New Zealand white rabbits

In papers 3 to 5, the Nuclear Microscopy techniques are used to investigate the role of trace elements in atherosclerosis. The aim of the studies is to evaluate the effect of elemental changes caused by the iron chelator *desferal* on the development of atherosclerosis. Other experimental trials are also described in this chapter to give an overview of the programmes carried out in CIBA on atherosclerosis study.

4.1 Overview introduction of atherosclerosis

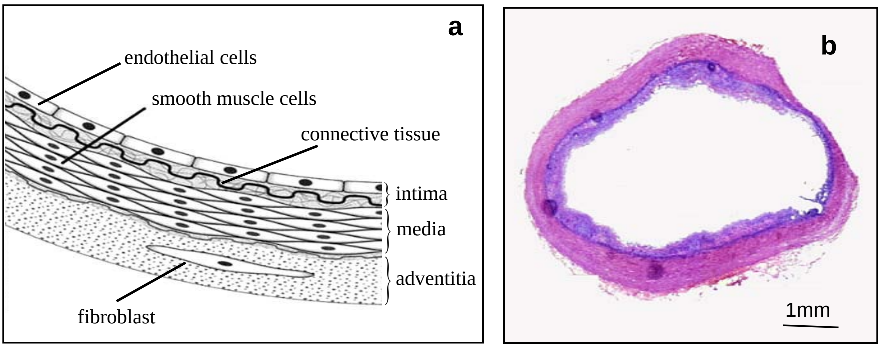

Figure 4.1: (a): Artery wall: schematic representation (after Wikipedia), (b): Hematoxylin & Eosin stained section of a rabbit aortic arch after 8 weeks on a high (1%) cholesterol diet. Rabbits on such a diet will start to develop lesions (purple color stained part) after 4-6 weeks.

Atherosclerosis is characterized by a buildup of fatty deposits on the inner walls of the affected arteries (see for example Figure 4.1), beginning with fatty streaks containing lipid-engorged macrophages [Ross99]. The arterial wall consists of four layers - the adventitia, the media, the intima and the endothelium (Figure 4.1). It is believed that the endothelial dysfunction is the very first step of atherosclerosis, and as a result, the permeability and the adhesiveness of the endothelium increases and it becomes easier for monocytes to adhere onto the surface of the endothelium. Subsequent effects such as macrophage formation and foam cell formation eventually leads to the formation of a lesion. Initially the artery tries to compensate by dilation (a process called remodeling), but as soon as it reaches a critical point, the plaque starts growing towards the lumen resulting in alteration and obstruction of the blood flow [Lusi00]. The most dangerous aspect is the rupture of plaques, which can block the blood flow, leading to myocardial infarction or stroke.

Advanced atherosclerotic lesions contain metal ions (e.g., iron and copper), which may be catalytic for free radical reactions [Smit92], although their role in early atherosclerosis development is uncertain [Dean00]. Several epidemiological studies have suggested that elevated tissue iron levels may increase the risk of atherosclerosis [Sull89, Ponk98, Sal95], although there are some contrasting views [Rossi00, Dane99]. Iron may be deleterious because of its ability to catalyze ***free radicals*** reactions [Hall84, Hall99] through the ***Fenton reaction*** and the process can be expressed as:

$$
\begin{gathered}
H_2O_2 + Fe^{2+} \rightarrow OH^{\cdot} + OH^{-} + Fe^{3+} \\
O_2{}^{\cdot -} + Fe^{3+} \rightarrow O_2 + Fe^{2+}
\end{gathered}
$$

These two reactions effectively sum up to give the ***Haber Weiss reaction*** (below), which is much faster in the presence of ferrous iron compared with that in a healthy biological environment.

$$O_2{}^{\cdot -} + H_2O_2 \rightarrow O_2 + OH^{\cdot} + OH^{-}$$

The ***free radicals*** like OH^- and $O_2^{\cdot -}$ generated will cause oxidative damage to the cells and surrounding tissues and eventually induce age-related diseases, such as atherosclerosis discussed in this chapter, as well as Parkinson's disease discussed in chapter 5.

Previous work has indicated that iron-dependent oxidative damage plays an important part in atherosclerosis development [Gile93, Stad04]. We have have already seen that when rabbits are fed on a high cholesterol (1%) diet, atherosclerotic lesions develop in the aorta after around 6 weeks, and these early lesions exhibit iron concentrations around seven times higher than those in the adjacent artery wall [Watt01]. In addition, we have found that venesection to induce mild anaemia before feeding cholesterol decreases the progression of atherosclerosis in the aortas of cholesterol-fed rabbits, in parallel with decreased lesion iron content [Ponr99].

Further evidence that iron is linked to atherosclerosis development is provided by the observation that treatment with the antioxidant iron chelator, desferrioxamine (Desferal®) [Hall89] produced a significant decrease in lesion area after 12 weeks [Ren05]. We also observed that for each individual animal, the localized lesion iron concentrations were positively correlated with the atherosclerotic lesion depth, whereas the localized zinc concentrations were inversely correlated with lesion depth, suggesting that zinc might have anti-atherogenic properties. Based on this interesting result, a study of zinc supplement was carried out using nuclear microcopy to investigate the role of zinc in the development of atherosclerosis [Ren06]. The results from this study showed that zinc supplementation markedly retards atherosclerotic lesion development in rabbits fed on a high cholesterol diet and accurately compared the iron levels in the lesion area between Zn-fed group (32ppm) and control group (43ppm). This is consistent with reports from other researchers that zinc has antioxidant and anti-atherosclerotic effects [Henn96, Bray90].

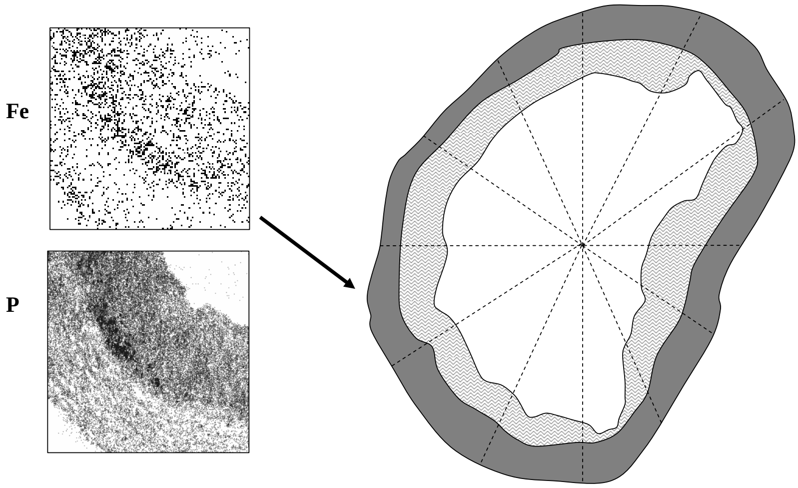

Figure 4.2: Schematic diagram of iron concentration measurements. The lesion section is divided into approximately 12 segments, and elements (including iron) are mapped within these regions. Accurate concentrations can be extracted from these maps both for the lesion and the artery wall. Shown above is the iron map from one segment, together with the phosphorus map. The phosphorus map indicates the boundaries of the lesion since this region is rich in phospholipids. Where the lesion varied in depth over the segment, the average depth of the lesion is measured.

4.2 Experimental trials

So far, there have been several experimental trials carried out using nuclear microscopy to investigate the correlation between trace elements (especially iron and zinc) and atherosclerotic lesion development in rabbits in CIBA. They are listed below:

- ***The effect of high cholesterol diet*** [Thon96]:

  New Zealand white rabbits were fed with 1% high cholesterol diet for 12 weeks. The aorta of 6 test and 4 control rabbits (on normal diet) were removed for the lesion elemental concentration analysis. Results show that there is an average of seven-fold increase in iron and an average of nearly two-fold increase in phosphorus in the atherosclerotic lesion compared to the healthy tissue. The increase in iron adds weight to the hypothesis that iron-catalyzed free radical reaction may be associated with the development of atherosclerosis.

- ***The effect of keeping the rabbit anemic*** [Ponr99]:

  A total of 27 male hybrid rabbits were used and divided into three groups: normal group (rabbits on standard rabbit chow diet), cholesterol-fed group (rabbits on 1% cholesterol diet and sacrificed after 4, 8, 12 and 16 weeks in groups of three) and bled cholesterol-fed group (rabbits on a 1% cholesterol diet and were subjected to weekly bleeding (15ml/week) and killed after 4, 8, 12 and 16 weeks in group of three). Results show that the beginning of early lesion was apparent in the 8-week cholesterol-fed rabbit but not in the 8-week bled cholesterol-fed rabbits. The calcification process is more advanced in the 16-week cholesterol-fed rabbit than in the 16-week bled cholesterol-fed rabbit. There is no increase in iron observed from the 8-week bled cholesterol-fed rabbit whilst iron accumulation is evident in the 8-week cholesterol-fed rabbit.

- ***The effect of implanting an osmotic pump with desferal - an iron chelator*** (paper 3 & 4):

  Sixteen New Zealand white rabbits were fed a diet of 1% high cholesterol food (Glen Forrest Stockfeeders, Western Australia). Six weeks into the diet, the rabbits were each surgically implanted with Alzet osmotic pumps (Alza Corporation, Palo Alto, CA, USA) containing desferal (0.5 g/ml) for the test group (8 rabbits), and saline for the control group (8 rabbits). The administered dose per rabbit (50 mg/kg body weight) is based on the published dose of 20 to 60 mg/kg used for treating iron overload in humans [Hall89]. Results show that desferal-induced iron chelation applied 6 weeks into the cholesterol diet for a period of 2 weeks does not slow the lesion development, but when applied for a period of 4 weeks indicates a possible trend ($p < 0.07$) to the reduction of lesion progression. This effect may be due to limited Fe chelation and raises the possibility that a further period of treatment might produce a significant reduction, this was the reason that the next trial was carried out (paper 3).

In this study, detailed investigations were carried out to map the localized iron concentrations within the lesioned tissue around the inner artery wall. Sections taken from three animals from the 10 week test group and three animals from the 10 week control group were scanned using the nuclear microscope. The iron concentrations were extracted for approximately 12 radial segments for each section of artery (see Figure 4.2 for details). The lesion iron levels for each radial segment were plotted against the average depth of the lesion in that segment. Pearson correlation analysis of the data shows a strong significant correlation between iron levels and the depth of lesion for both the test groups and control groups, but a clear inverse correlation for zinc except in one animal. These graphs also further illustrate the high variability in iron and zinc levels and lesion areas between animals [Ren03] (paper 4).

- ***The effect of desferal injection*** (paper 5):

  New Zealand white rabbits were fed with a 1% w/w cholesterol diet for either 8 weeks (with the last 5 weeks injected daily with desferal), or for 12 weeks (with the last 9 weeks injected with desferal). Controls were injected with saline. A significant reduction in average lesion area (p=0.038) was observed in the 12-week treated animals as compared to the 12-week controls. The average lesion iron level of the 12 week treated animals (58 ppm dry weight) was significantly lower ($p = 0.03$) than for the 12-week control animals (95 ppm dry weight). No reduction in lesion area or iron content was observed in the 8 week treated animals compared with controls, and no change in lesion zinc concentration was observed for either group. This data is consistent with the concept that iron contributes to the early stages in the development of atherosclerosis and that removal of iron from the lesion retards the progression of the disease [Ren05] (paper 5).

- ***The effect of zinc supplementation*** [Ren06]:

  The rabbits in the test group received a 1% w/w cholesterol diet with Zn supplements for 8 weeks and the rabbits in the control group were fed only with a 1% w/w cholesterol diet for the same period of time. Lesion area analysis using light microscopy showed that the average lesion area was 1.0 mm^2 for the test models compared with 3.0 mm^2 for the control group models ($P = 0.0045$). Elemental analysis of the lesion and adjacent artery wall revealed that the average zinc level remained the same for both the lesion and the artery wall for all the test and control models, whilst the iron levels are reduced from 43 ppm to 31 ppm (in the lesion) and from 17 ppm to 6 ppm (wt., in the artery wall). This raises the possibility that zinc may act as an endogenous protective factor against atherosclerosis by reducing iron levels.

I have actively taken part in the work carried out for the last three experimental trials.

4.3 Materials and methods

- ***Animal models***: Male New Zealand White rabbits were fed a 1% high cholesterol diet (*Glen Forrest Stockfeeders, Western Australia*) to induce atherosclerosis as both control models and test models with different experimental trials as mentioned above.
- ***Tissue blocks studied***: Rabbits were sacrificed by i.v. injection of sodium pentobarbitone (0.8 mg/kg). The aortic arch was removed and cut into three segments A, B, and C (shown in Figure 4.3). Segments were flushed with deionized water to remove residual blood from the inner artery wall, and flash frozen in liquid nitrogen.
- ***Lesion area analysis***: 25 μm sections were placed on slides for H&E (hema-

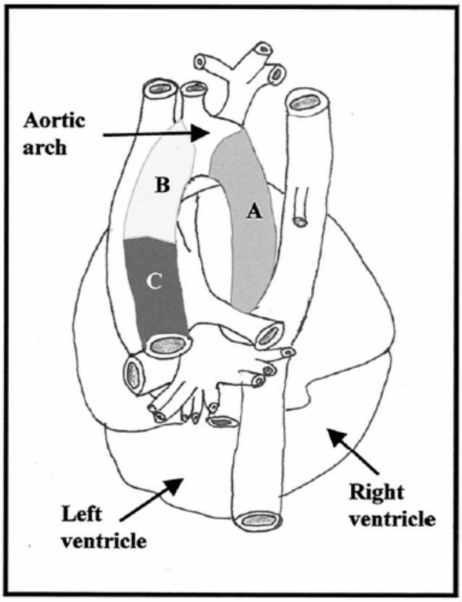

Figure 4.3: A schematic drawing of the heart showing the three segments of aortic arch.

toxylin and eosin) (Appendix B) staining before the evaluation of lesion development was carried out using the Carl Zeiss Axiophot II image analyzer utilizing the KS400 (version 3.18) analysis software.

- ***Nuclear Microscopy analysis***: Elemental analysis on unstained sections (thickness: 14 μm) of tissue was carried out using the CIBA Nuclear Microscopy facility [Watt94] using a 2.1 MeV proton beam focused to a 1 μm spot size, and utilizing three complementary ion beam techniques (PIXE, RBS and STIM) simultaneously.

4.4 Results and conclusions

The results from various experimental trials with regard to atherosclerosis show that iron is present in early lesions at concentrations around seven times higher than that in the artery wall. Measurement of localized lesion iron and concentrations shows that iron is highly correlated with the depth of lesion grown in the artery wall for each individual animal, implying that local elevated concentrations may accelerate the process of atherosclerosis in specific regions of the artery. When the rabbits were kept mildly anemic, the progression of the disease was significantly slowed down. Iron chelation using *desferal* showed that early treatment (three weeks into the high fat diet) for relatively long period of time (nine weeks) significantly inhibited the progression of the disease. Zinc is observed to be depleted in the lesion and inversely correlated with local lesion development. Feeding the rabbits on a high fat diet with zinc supplements greatly slowed down the lesion development. But there is no significant zinc increase in the lesion; this may indicate that the anti-atherosclerotic effect of zinc is indirect.

These results are consistent with the hypothesis that iron plays a role in atherosclerosis probably through the production of free radicals. Our data support the concept that zinc may have an antiatherogenic effect by decreasing iron levels in the lesion, possibly leading to inhibition of iron-catalyzed free radical reactions.

Further work is on the way to investigate the cellular and tissue iron contents with the induction of a specific protein, called haem oxygenase-1 (HO-1). Haem oxygenases catalyze the oxidative cleavage of iron protoporphyrin IX (haem) to carbon monoxide, iron, and biliverdin that is subsequently reduced to bilirubin by biliverdin reductase. Of the three isoforms, inducible HO-1 and constitutive HO-2 are expressed in the vasculature. The best-established in vivo function of HO-1 is its anti-inflammatory activity, and this may be of direct relevance to cardiovascular disease (CVD) including atherosclerosis. HO-1 plays an important role in iron homeostasis, as HO-1-deficient mice develop anaemia associated with accumulation of tissue iron thought to contribute to oxidative damage, tissue injury, and chronic inflammation [Poss97].

There is strong and increasing support for increased HO-1 activity protecting against atherosclerotic vascular disease. [Wang98, Ryt06].

5 Trace elements and Parkinson's disease in primates

In papers 1 and 2, Nuclear Microscopy techniques have been applied to study the distribution and concentration of elements in the brains of primates where Parkinson's disease has been induced. The goal of the study is to see if this disease could be associated with changes in the trace element distribution and concentration.

5.1 What is Parkinson's disease?

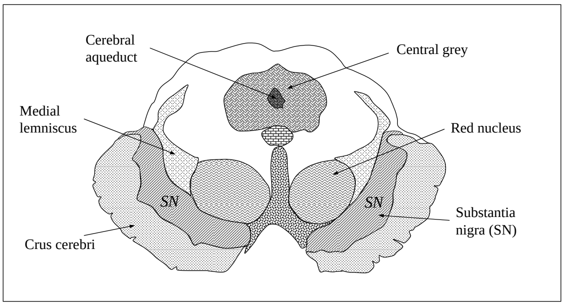

Figure 5.1: A transverse section of the mesencephalon at the level of the superior colliculus.

Parkinson's disease (PD) is a progressive neuronal degenerative brain disease of the elderly and is caused by the selectively degeneration of neurons in the Substantia Nigra (SN)(Figure 5.1) region of the brain. The commonly recognized conditions are marked by a characteristic set of symptoms among which are trembling of the limbs, muscular stiffness and slowness of the bodily movement. These symptoms reflect the dysfunction of the Substantia Nigra (SN). The SN region is packed with neurons that can produce and store the chemical neurotransmitter dopamine, which acts as a chemical messenger transmitting signals to other nerve cells in the dorsal striatum - the deep grey matter of the cerebral hemispheres. When SN nerve cells are injured, or for some reason cannot produce or store dopamine, a dopamine deficiency in the striatum results and if this is sufficiently severe, symptoms of Parkinsonism begin to appear. By the time of diagnosis, that is generally when movement disorder symptoms first appear, patients with PD have lost 70% of their dopaminergic neurons.

Parkinson's disease has been known for 190 years since it was first described in 1817 [Park17]. Aging is a significant risk factor for the development of Parkinson's disease, with the average onset around 60 years old [Duvo95].

The hypothesis concerning the pathogenesis of PD is that there is ongoing, selective oxidative stress (OS) that expresses itself as biochemical alterations compatible with this state [Gerl94, Gotz94, Jenn98]. The degeneration of the dopaminergic neurons is believed to be associated with an excess of highly reactive oxygen species such as hydroxyl (OH^-) and superoxide ($O_2^{\cdot -}$) radicals [Sofi92, Youd93]. The role of iron as an aetiological factor was suggested when it was discovered that iron was elevated by about 77% in the Substantia Nigra pars compacta (SNc) of human parkinsonian brain [Sofi88]. Here experiments carried out using parkinsonian rat and monkey models seem to support such a hypothesis [He96, Thon97]. The excess iron may facilitate the reduction of hydrogen peroxide (H_2O_2) (e.g. see section 4.1) derived from the oxidation of dopamine by monoamine oxidases and from the mitochondrial electron transport chain to highly cytotoxic hydroxyl radicals [Thon99].

5.2 Animal model of Parkinson's disease

There are two neurotoxins that produce animal models of oxidative stress and parkinsonism syndrome in rodents, primates and other species. Both neurotoxins, namely 6-hydroxydopamine (6-OHDA) [Kost74] and MPTP (N-methyl-4-phenyl-1,2,3,6-tetrahydropyridine) [Burn83, Davi79] cause the degeneration of nigro-striatal dopaminergic neurons, with the subsequent loss of striatal dopamine. The consequence of oxidative stress is the initiation of reactive oxygen species (ROS) generation, followed by brain membrane lipid peroxidation. MPTP provokes a progressive Parkinsonism in humans which includes all important clinical features of PD, except for the presentation of Lewy bodies, which are abnormal aggregates of protein that develop inside nerve cells [Lang96]. This is thought to initiate its dopaminergic neurotoxicity via metabolism catalysed by monoamine oxidase (MAO), giving rise to its reactive metabolite MPP+. The latter is thought to begin the neurodegeneration process via reactive oxygen species induced oxidative stress and inhibition of mitochondrial complex I [Sing87, Seat97] as it produces sustained dopamine oxidation, hydroxyl radical formation and membrane lipid peroxidation [Chiu92].

In our study, a total of 6 adult macaque monkeys (*Macaca fascicularis*) weighing 1.1 - 3.7 kg were used. The ages of the monkeys were estimated by a trained veterinary surgeon using the characteristics of weight, the amount of wear on the dentition, and from facial photographs. They were then classified into two groups: young monkeys weighing 1.1 - 1.3 kg, and aged less than seven years, and monkeys weighing 3.5 - 3.7 kg, and aged over seven years.

All the monkeys were unilaterally lesioned (right side) with MPTP and housed individually under natural day-night cycle conditions and provided with food and water. The left (unlesioned) Substantia Nigra in each case was used as a control. The subjects were all sacrificed five weeks after MPTP injection, a time interval known from our previous experiments to correspond to an approximate average neuron cell death of 40 - 50% in the lesioned SN.

5.3 Special staining procedure carried out on NM target holders

The procedure for collecting the brain sample blocks and how the sectioning was carried out are described in detail in the relevant papers (paper 1 & 2) attached in this thesis. The blocks were sectioned at 20μm thickness using a freezing microtome (Jung Frigocut 2800E) operating at -17^0C object temperature and - 22^0C box temperature. The sections were grouped into four sets as follows:

- The first set of sections was mounted on glass slides, and standard Nissl staining (a histological stain which was used for selective visualization of neuronal cell bodies throughout the brain, more details in Appendix C) was carried out for cell identification and cell counting in both the right, lesioned, and left, non-lesioned, Substantia Nigra. The characteristic large diameter neurons with abundant Nissl substance, characteristic of dopaminergic neurons in the Substantia Nigra, were counted.
- The second set of sections was mounted on nuclear microscope holders supported on sub-micron pioloform film (a self-supporting plastic film used in nuclear microscopy studies), and air-dried. These (unstained) sections were used for accurate measurements of the iron concentrations using nuclear microscopy.
- The third set of sections was mounted on nuclear microscope holders and air-dried. These sections were Nissl stained, and the iron distribution mapped with nuclear microscopy using the same section to determine any correlation between the location of iron and that of neurons. Previous scans on unstained and stained tissue have indicated that the iron distribution, particularly that of focal deposits of iron, is not significantly affected by the Nissl staining process. Standard Nissl

staining procedures were used, except that the dehydration step using xylene was omitted because of its chemical reaction with the pioloform support film. Immunocytochemical staining for dopamine or tyrosine hydroxylase was not carried out, as these multiple-step procedures needed might interfere with the very sensitive, nuclear microscopic measurements of iron.

- The fourth set of sections was cut in order to ascertain the possible presence of ferrous iron using Turnbull's blue staining. This staining was carried out by following a protocol described previously [McMa60]. The sections were mounted on glass slides and fixed using a solution of 4% paraformaldehyde in phosphate buffer pH 7.4 for 20 minutes. They were then washed in distilled water and immersed in a potassium ferricyanide mixture (containing 1 part of 2% potassium ferricyanide and 1 part of 2% hydrochloric acid) for 30 minutes, followed by washing with distilled water for 6 times at 5 minutes each.

5.4 Results

The results have been drawn from the stained sections and unstained sections from the following aspects:

- ***Cell counts from the first set of sections:*** (paper 2)

  The number of neurons remaining on the side of the MPTP injections was reduced compared with the contralateral (control) non-lesioned side. A trend towards increased cell loss after MPTP injection was observed in the younger monkeys, compared to older monkeys, although the difference was not statistically significant. In monkeys aged greater than 7 years, an average of 36% cell loss was observed, whereas in monkeys aged less than 7 years, an average of 56% cell loss was observed.

- ***Elemental concentration from the second set of sections:*** (paper 1)

  Areas encompassing many regions of the midbrain from the 3 young and 3 old monkeys were scanned using nuclear microscopy with the combination of STIM, RBS and PIXE. Several regions of interest were analyzed using the playback function of the list-mode files for their iron content. Iron levels in the Substantia Nigra, red nucleus and the cerebral peduncles were obtained. The average iron concentrations in the Substantia Nigra of the old monkeys was five times elevated compared to that of the young monkeys (significance: $p < 0.05$). For the red nucleus and the white matter, the elevation in iron levels for young and old monkeys was 1.2 and 1.5 times, respectively. These differences were, however, not statistically significant. No significant difference in iron levels was found between the lesioned and the non-lesioned sides, for the three areas analyzed.

- ***Iron distribution in the substantia nigra (Nissl stained sections on NM target holders):***(paper 1)

  The sections on the NM target holders subjected to the Nissl staining procedure were air-dried and many optical images were taken to analyze the neuron body distribution before the sections were scanned for elemental (especially iron) distribution to determine the correlation with the neurons. During the nuclear microscopy measurement, STIM was very useful to rapidly position the area of interest within few minutes. As seen in Figure 5.2, areas containing high iron concentrations appear as closely-spaced dots, whereas those containing lower iron concentrations are represented as less closely-spaced dots under nuclear microscopic scans. In young monkeys, the iron appeared fairly uniformly distributed and showed little evidence of focal deposits. A close comparison between iron distributions in nuclear microscopic scans and cell distributions in sections stained by the Nissl technique, however, showed some areas containing higher iron concentrations. These were present, not where densely-packed large cell bodies (presumed dopaminergic neurons in the pars compacta) were located, but rather, in areas away from the cell bodies (Figure 5.2 A,B). These distributions were present on the control side as well as the MPTP-injected side.

  The substantia nigra of old monkeys showed not only an increase in iron levels but also the appearance of a large number of focal deposits of iron. There was also a much more obvious "inverse correlation" between the distribution of iron and neuronal cell bodies in these monkeys. Areas of high iron concentrations were observed, which contained focal accumulations of extremely high densities of 'dots'. As in the younger animals, the iron-rich areas were present not where densely-packed large cell bodies (presumed dopaminergic neurons in the pars compacta) were located, but rather, in a region ventral to these cell bodies i.e. in the pars reticulata. These distributions were as in the case of young monkeys present on the control side (Figure 5.2 C,D) as well as the MPTP injected side (Figure 5.2 E,F), implying that they were present before MPTP injections.

- ***Ferrous iron distribution (fourth set of sections):*** (paper 2)

  There was absence of ferrous iron staining on both the lesioned and non-lesioned sides in young monkeys (Figure 5.3 A). In contrast, focal deposits of ferrous iron granules were observed in the Substantia Nigra of both the lesioned and non-lesioned sides in all three old monkeys (Figure 5.3 B). Ferrous iron was not observed in any other regions of the midbrain of any of the 6 monkeys. The result on ferrous iron is consistent with measurements carried out using synchrotron radiation X-ray fluorescence Spectroscopy (SXRF) and Fe K-edge X-ray absorption near-edge structure (XANES) [Ekte04]. Nuclear microprobe analysis without using a high-resolution wavelength dispersive spectrometer is unable to provide the information on elemental status. However, even then it is questionable if sufficient sensitivity can be realized from the X-ray fine structure.

5.5 Conclusions

The study of Parkinson's disease was aimed at using the nuclear microscopy techniques to elucidate the iron concentration and distribution in the SN of both young and old primates following unilateral MPTP-lesioning. Nuclear microscopy measurements were carried out both on unstained flash frozen tissue sections to extract iron concentrations in the SN, and on Nissl-stained tissue sections to aid a direct comparison between the iron distribution and SN neuron location.

A significant difference (from 233 to 1092 ppm) in iron concentrations between the SNs of young and old primates was observed. When comparing the lesioned and non-lesioned SNs of the same animal, we found no significant difference in iron levels for each young primate, and a slight increase in iron ($\sim 10\%$) between the lesioned SN and control SN for old primates. These results are consistent with our previous work showing that there may be an increase in the iron concentrations at an early stage if there are iron-rich deposits present in the SN [Thon99]. The presence of iron-rich deposits in the SN (both lesioned and control) was observed in all old primates, this is in contrast to the SNs of young primates where these focal deposits were rarely observed.

These results appear to indicate that in primates the SN iron levels increase with age, and that a substantial fraction of the increased iron is in the form of iron-rich granules. This iron-rich granule does not appear to be co-localised with other trace elements (e.g. Al, Cu, Ca and Zn etc.). A 200 μm scan over an iron granule rich area of the brain section was performed and Figure 5.4a is the iron distribution map showing the presence of iron-rich granules. They were observed in all of the older primates both in the lesioned and non lesioned Substantia Nigra (SN), but very few granules were found in any of the young primates. Figure 5.4b shows a typical PIXE spectrum of an iron rich granule which shows the absence of other trace elements except Fe. This result is different from previous observations by other groups [Schi98, Good92] which used different analytical techniques. Our result however is consistent with a research work carried out using synchrotron EXAFS which indicates that the increased iron in the parkinsonian SN is stored in a relatively pure form such as ferritin [Grif99].

A novel observation in this work is the inverse correlation between the iron distribution and the SN neuron locations. The inverse correlation is weak in young primates where no iron-rich granules were observed, but more pronounced in the older primates where there is a proliferation of iron-rich deposits. This result indicates that neuronmelanin, which was believed to be the iron sequestration sites [Thon99, Good92], may not be the major sites for the accumulation of SN iron with age. Our previous work has shown that iron accumulation can be observed in the glial scars in the kainate-lesioned hippocampus [Ong99]. Other works have identified iron deposits in microglia, neurons, oligodendrocytes and neuropil [Schi98, Fran81, Hill84].

These studies, together with the observed anti-correlation between iron and neuron distributions in our work, tend to suggest that the majority of focal iron is stored in the microglia as ferritin granules, although more work needs to be done to confirm this hypothesis. However, it is possible that increased loading of iron granules in SNs, particularly at the extremely high levels observed in this work, may precipitate free radical production and neuronal damage.

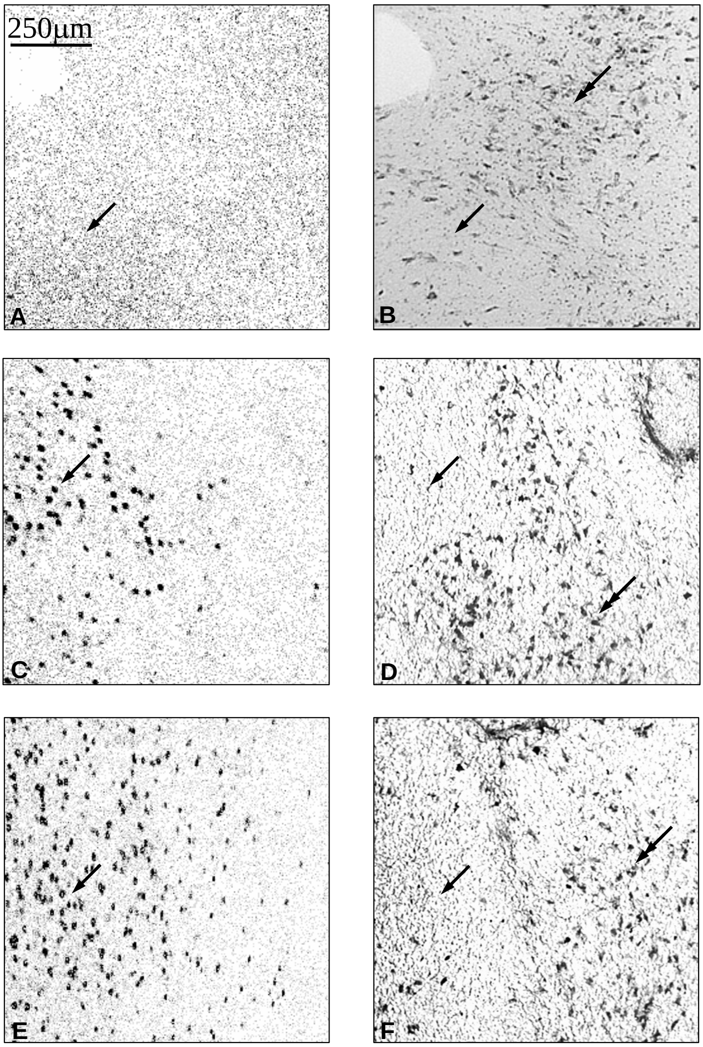

Figure 5.2: Iron distribution in the substantia nigra. A, B: iron (A) and Nissl stained (B) map of the same section, from the lesioned side of a young monkey. There are no focal deposits of iron in this and the other two animals in this group. An area of slightly higher density of iron is visible (arrow in A), but this region is away (arrow in B) from the location of large neuronal cell bodies (arrow in B) with abundant Nissl substance, and characteristic of Type I dopaminergic neurons. Immunocytochemical staining for tyrosine hydroxylase was not carried out, as it could interfere with the nuclear microscopic measurements of iron. C, D: iron (C) and Nissl stained (D) map of the same section, from the non-lesioned side of a monkey aged greater than 7 years. Focal deposits of iron are observed even in the unlesioned side (arrow in C). Their location is away (arrow in D) from large neurons with abundant Nissl substance (double arrow in D). E, F: iron (E) and Nissl stained (F) map of the same section, from the MPTP-lesioned side of an old monkey. As in the unlesioned side, focal deposits of iron (arrow in E) are present away (arrow in F) from large neurons with abundant Nissl substance (double arrow in F).

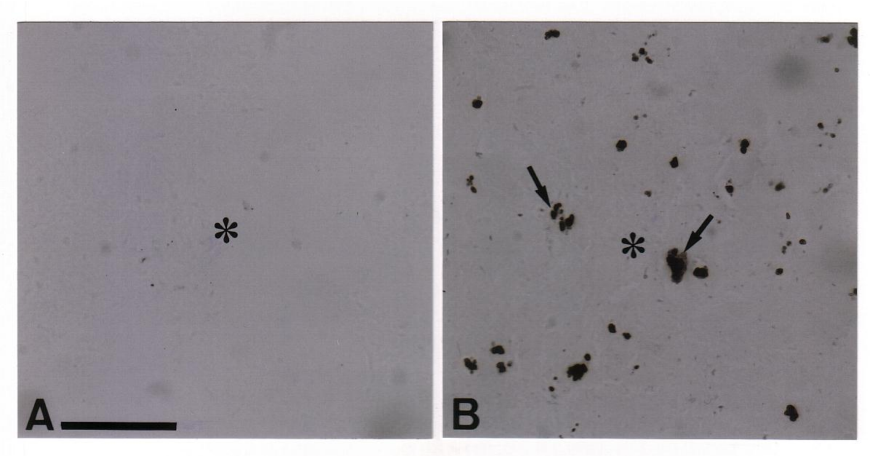

Figure 5.3: Sections of the substantia nigra on the MPTP-lesioned side (asterisk), stained by Turnbull's blue stain for ferrous iron deposits. A: young monkey, showing lack of ferrous iron deposits. B: old monkeys, showing presence of ferrous iron deposits (arrows). Scale bar = 150μm.

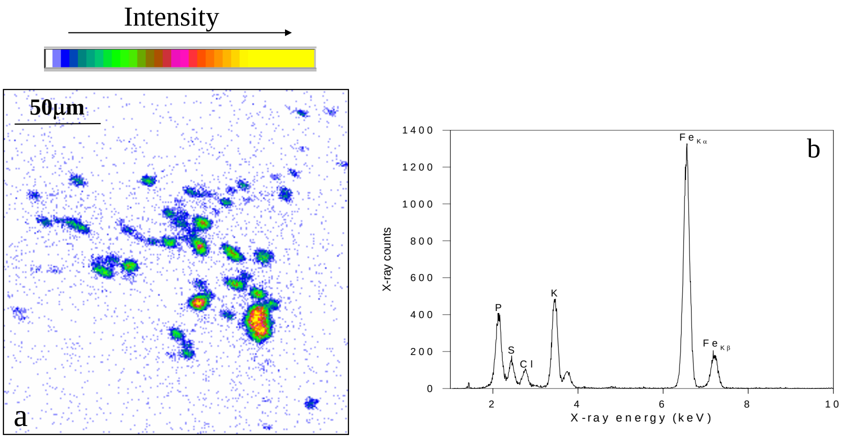

Figure 5.4: (a) Iron distribution map showing the presence of iron-rich granules, (b). A typical PIXE spectrum of an iron rich granule (2.1 MeV proton beam, 300 μm perspex filter with a 1 mm central hole.)

6 Quantitative Nuclear Microscopy in materials physics research

Some Nuclear Microscopy investigations in materials research that focus on the direct STIM technique are presented in papers 6 to 8. RBS and direct STIM techniques have been used in the studies. This chapter will explain in detail the use of the Si PIN diode as a STIM detector, a substrate for cell imaging and for a stopping medium thickness measurement.

6.1 Silicon Pin-diode

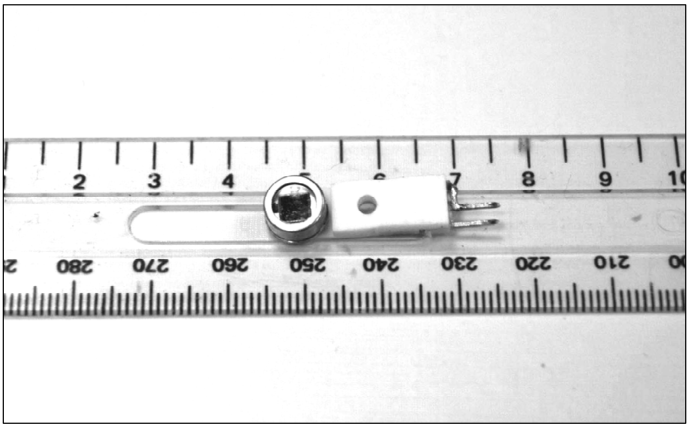

Figure 6.1: Silicon PIN photodide (purchased from Hamamatsu) used in our studies.

Si PIN photodiodes (shown in Figure 6.1) are capable of high-speed response when operated with a reverse bias and for this reason are widely used for optical communications and optical disk pickups, etc. They have also been used for radiation detection

[Yama84, Erem87, Good87], and because of their small size and high quantum efficiency (∼ 80%), they have been used in place of photomultiplier tubes in experimental apparatus where space is limited [Govl03]. Investigations carried out with PIN diodes show that these detectors have extremely low leakage current and low noise.

Hamamatsu Si PIN photodiodes (model S1223-01) have been employed as ion energy detectors in our work. These PIN diodes have an active area of 3.6 × 3.6 mm on a TO-5 header and low dark current (∼ 0.2 nA) [Hama01]. In each case the cap has been removed and the diodes used as a STIM detector, a substrate for growing cells and coated directly with a patterned layer of the stopping medium for stopping force measurement. It is notable that the low cost of these PIN diodes (around 10 US$) enables disposable use of these detectors that would be economically prohibitive with conventional detectors.

6.2 Direct imaging of cells grown on Si_3N_4 window using a pin diode

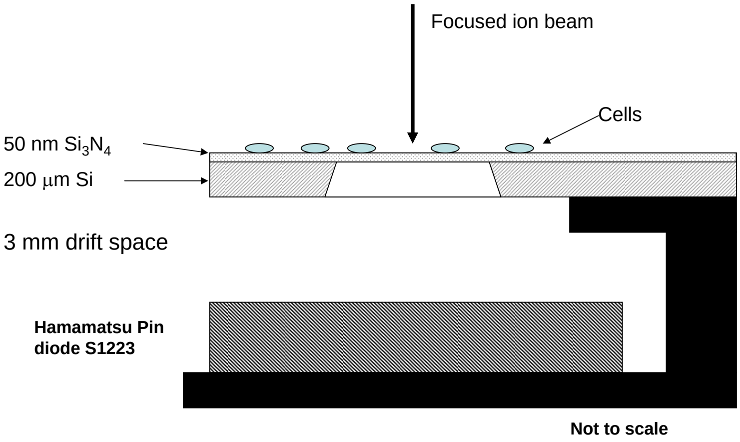

Figure 6.2: Schematic diagram of the STIM assembly, showing the silicon nitride window and the pin diode. The cells are grown on the upper surface of the Si_3N_4 window.

It was mentioned in chapter 2 that the CIBA proton beam writing beam line can routinely focus MeV ion beams to sub-100 nm dimensions. The target chamber however is not readily amenable for either STIM or nuclear microscopy investigations, because the short target stage to lens distance (working distance) is only 7 cm compared to 15 cm in the CIBA nuclear microscopy line [Watt03]. This limits the space available for microscopes and detectors. In order to adapt to the reduced working distance, a miniature STIM assembly was constructed based on a Hamamatsu pin diode S1223-01 (3.6 × 3.6 mm chip) mounted on an assembly fronted by a silicon nitride window of thickness 50 nm (shown in Figure 6.2). This STIM assembly was mounted on a computer-controlled Burleigh Inchworm EXFO XYZ stage which has a travel of 25 mm for all axes with a 20 nm closed loop resolution [Van03].

The cells used were MCF-7 American Type Culture Collection [ATCC] breast cancer cells and they were prepared according to the protocol described in Table 6.1. This procedure is commonly used for scanning electron microscopy in cell biology to preserve the structural integrity of cells. It can be seen in Figure 6.3 that the cells were successfully grown on the 50 nm thick silicon nitride window.

Culturing of the breast cancer cells:	MCF-7 breast cancer cells (American Type Culture Collection [ATCC HTB-22]) were maintained in Dulbecco's modified Eagle Medium (DMEM, Sigma) supplemented with 10% fetal bovine serum (FBS, Hyclone) at 37^{0}C in a humidified atmosphere (95% air and 5% CO_2). Cells were subsequently harvested by trypsin treatment and seeded on the silicon nitride substrate.
Processing of cultured cells:	The silicon nitride window was first UV sterilized (30 minutes) and the cells plated on to the window. The culture medium was removed and the cells given a quick wash with Phosphate Buffer(PB)(0.1M, pH7.4). Cells were then fixed with 3% Glutraldehyde (pre--pared in 0.1M PB, pH 7.4) for 1 hr. The fixative was then removed and cells washed with PB - 5 min (3×). The cells were then passed through a series of ethanol dehydration steps: 25% -3min, 50% -3min, 75%, -3min, 95% -3min, 100% -5min, 100% -5min.
Critical point drying:	The samples were transferred into the Critical Point Dryer (BAL-TEC CPD 030) and dried for about 1 hour. Samples were placed in small porous containers to ensure they were not damaged during the drying process. The pressure was released slowly after drying to avoid rupturing the 50 nm silicon nitride window.

Table 6.1: Cell preparation protocol.

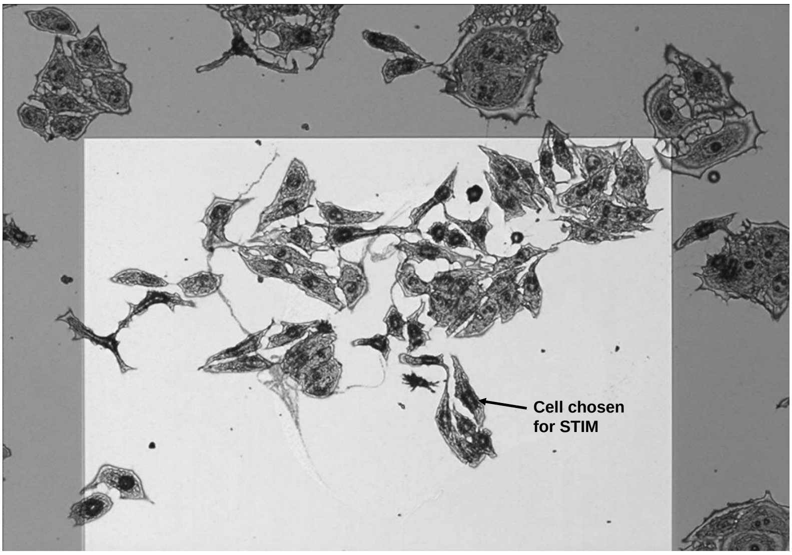

Figure 6.3: Optical micrograph of the breast cancer cells grown on a 50 nm thick silicon nitride window (500 μm x 500 μm). The cell chosen for the STIM studies is marked in the figure. The light region is the open area of the Si_3N_4 window.

A 2 MeV H_2^+ beam (equivalent to 1 MeV proton beam) and a 1 MeV alpha beam were used and focused to sub 100 nm and scanned across the same cell indicated in Figure 6.3. The STIM spectra from the cell for both the H_2^+ and the alpha beam were collected by the Hamamatsu PIN diode positioned directly behind the window and operating at 10 volt reverse bias voltage. It can be seen from the STIM energy spectra shown in Figure 6.4 that H_2^+ suffers little energy loss compared to the alpha beam traversing through the same cell grown on 50 nm Si_3N_4 window. This is expected because of the higher stopping power of 1 MeV alpha particles compared with 1 MeV protons (408 keV/μm for alpha particles and 52 keV/μm for protons in carbon calculated using SRIM [Zieg85]).

Estimates of the straggling of the protons and alpha beam traversing the 50 nm substrate window (1 keV for 1 MeV protons and 2.4 keV for 1 MeV alpha particles) were estimated using SRIM to be small compared to the detector energy resolution measured to be 23 keV for the 1 MeV alpha particles and around 27 keV for the 2 MeV H_2^+. Figure 6.5 shows that STIM images of the same cell bombarded by 2 MeV H_2^+

and 1 MeV alpha beam, and the images were collected and processed with OMDAQ using a median fit [Grim91]. It is evident that the STIM image using the alpha beam exhibits considerably higher contrast than the image using the H_2^+ beam, although in both cases the cell nucleus is clearly visible.

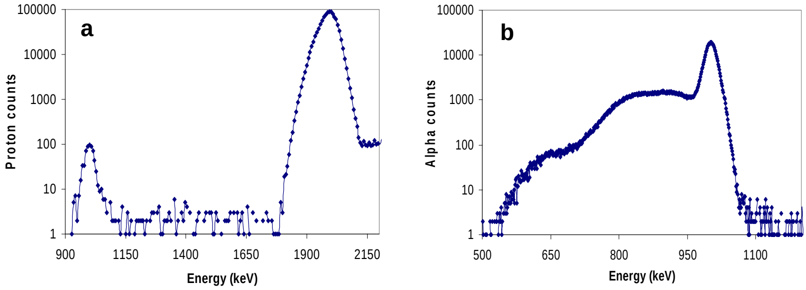

Figure 6.4: STIM energy spectra from a) 2 MeV H_2^+ beam penetrating the cell depicted in figure 6.3, and b) 1 MeV alpha beam penetrating the same cell.

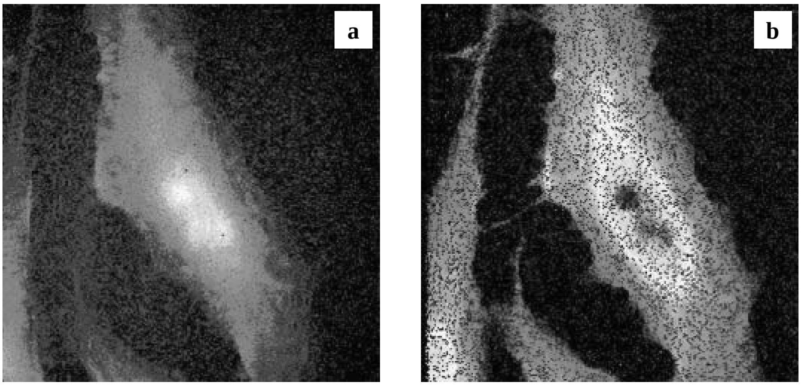

Figure 6.5: STIM images of the cell on the silicon nitride window as depicted in figure using a) 2 MeV H_2^+ beam and b) 1 MeV alpha beam. The scan size is 40 microns in each case and the STIM images have been assembled using a median energy fit.

Because the 50 nm silicon nitride window is very fragile and difficult to handle, it was decided to investigate the possibility of imaging the cells using silicon PIN diode directly as a cell-growth substrate. For doing this, two major issues were of concern:

growing the cells on the PIN diode and the damage to the PIN-diode by the incoming ion beam. As shown in Figure 6.6, growing the cells directly on the PIN diode by following the same protocol as described in table 6.1 proved to be remarkably successful, provided that the PIN diode was pre-sterilized using UV radiation. Autoclave sterilization led to corrosion of some parts of the TO-5 header. The cells were subjected to H_2^+ beam and alpha beam scanning and as expected, the alpha STIM exhibited more contrast than the proton STIM (shown in Figure 6.7).

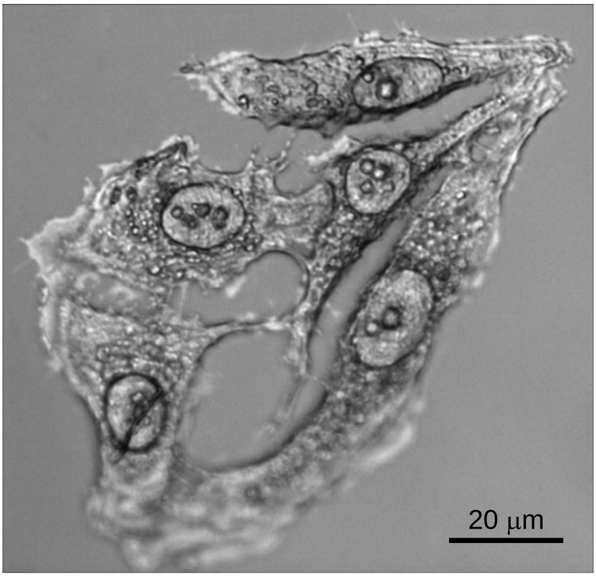

Figure 6.6: Optical micrograph of breast cancer cells plated on the PIN diode surface, showing a high degree of structural integrity.

As a further test of nano-STIM, a 1 MeV alpha beam was focused down to 80 x 90 nm (as measured by the new CIBA resolution standard [Zhan07], both before and after the scan), and scanned over the same cell depicted in Figure 6.7b with a reduced scan size of 15 × 15 microns. Each pixel in the 256 × 256 pixel image is calculated to be 60 × 60 nm, which is just slightly smaller than the beam spot size. The high magnification STIM image is shown in Figure 2.5, and the nucleus together with other smaller features are clearly observed. The second issue of beam damage is addressed in the following section.

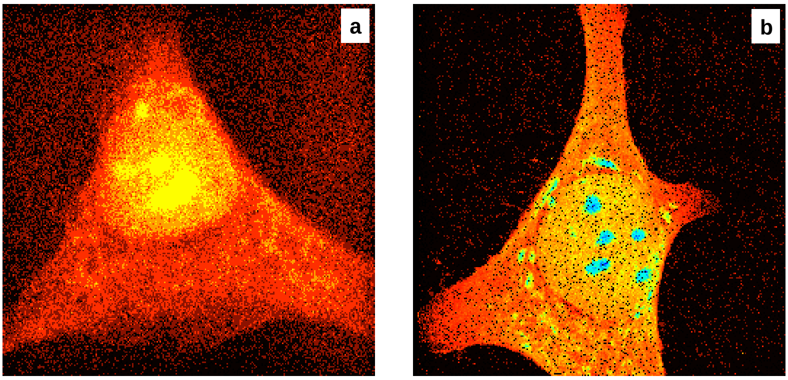

Figure 6.7: STIM images of cells grown directly on the PIN diode, using a) 2 MeV H_2^+ beam and b) 1 MeV alpha beam. The scan size is 40 μm in each case, and the STIM images have been created using a median energy fit.

6.3 Beam damage measurement

As the ion beam penetrates the depletion layer of the diode, atomic displacement damage results in the formation of trapping centers which in turn reduces the collection of charge induced by single ions. Detailed information about the precise effects and generating mechanisms of this damage build-up can be found in Refs [Sim05, Whit98]. Generally, we require the STIM image to be formed before the induced charge is reduced by an amount approximately equal to the energy resolution of the pin diode detector. In order to investigate the damage caused by the 1 MeV proton and alpha beam, two virgin (by beam) regions (40 x 40 μm) of the pin diode were selected and scanned using 1 MeV protons (2 MeV H_2^+) and 1 MeV alphas, and the data was recorded in list mode files, which enabled us to extract the position of the peak sequentially. The peak positions were plotted as a function of the number of ions per μm^2. Figure 6.8 shows results of these measurements.

It is seen from the graphs that the initial shift in energy due to damage created by the alpha beam (6.1 keV/(100 ions /μm^2) = 6.1 keV/(10^{10} ions/cm^2)) is higher than that from the protons (0.35 keV/(100 ions /μm^2) = 0.35 keV/(10^{10} ions/cm^2)). Our results are in reasonable agreement with the measurements reported earlier [Ague05, Maet99]. From the measurement and calculation carried out here, we can determine that for a typical STIM image (average 10 counts/pixel) with a pixel size of 50 nm, the requirement of 4000 counts per μm without incurring significant detector damage is just possible for proton STIM, whilst for alpha STIM, the obvious increase in detector damage is compensated by the energy loss in traversing through the cell. However, if the resolution requirement of certain experiment is better than 100 nm, there may be a need to apply a correction procedure to account for the accumulated alpha beam damage.

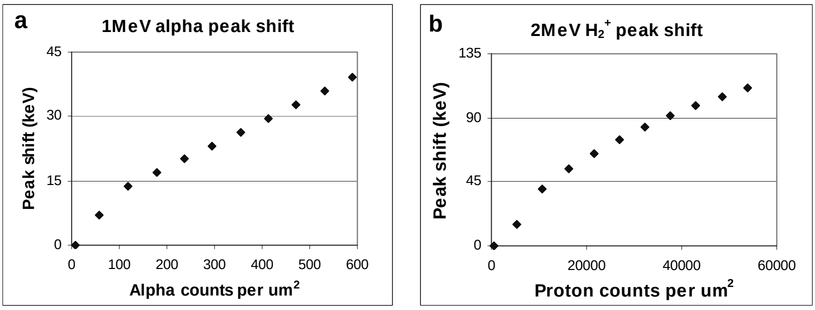

Figure 6.8: Peak energy shift caused by ion beam damage on a PIN diode from a) 1 MeV alpha particles, and b) 1 MeV protons (2 MeV H_2^+).

6.4 "Polka-dot" detector studies of stopping force

"Polka-dot" detectors are formed by coating a PIN photodiode with islands of a stopping medium arranged in a regular polka-dot pattern (shown in Figure 6.9a).

Hamamatsu Si PIN photodiodes (model: S1223-01) were also employed in this study. In each case, the cap was removed and the detector coated directly with a patterned layer of stopping medium by e-beam evaporation [Timm04]. Basically, the detectors were coated by evaporating the stopping medium (in our case, *Ge, Au and Ag*) of interest onto the active area of the diode through a 0.3 mm thick stainless steel mask with 500 μm diameter circular holes (shown in Figure 6.9b) that were produced by laser cutting. The mask was positioned approximately 1 mm above the detector surface in order to prevent the damage to the active layer of the detector during evaporation. Inspection with an optical microscope revealed that the pattern was accurately transferred to the diode surface (Figure 6.9c). The circular islands of stopping medium are flat and have well defined edges. Detectors coated with Ge, Au and Ag have been employed in our study, with different coating thicknesses in the range of 250 - 300 nanometres.

Subsequently polka-dot PIN photodiodes were employed for accurate stopping force measurements. These are especially useful for low-energy heavy ions where a very thin stopping medium is required to reach low ion energies.

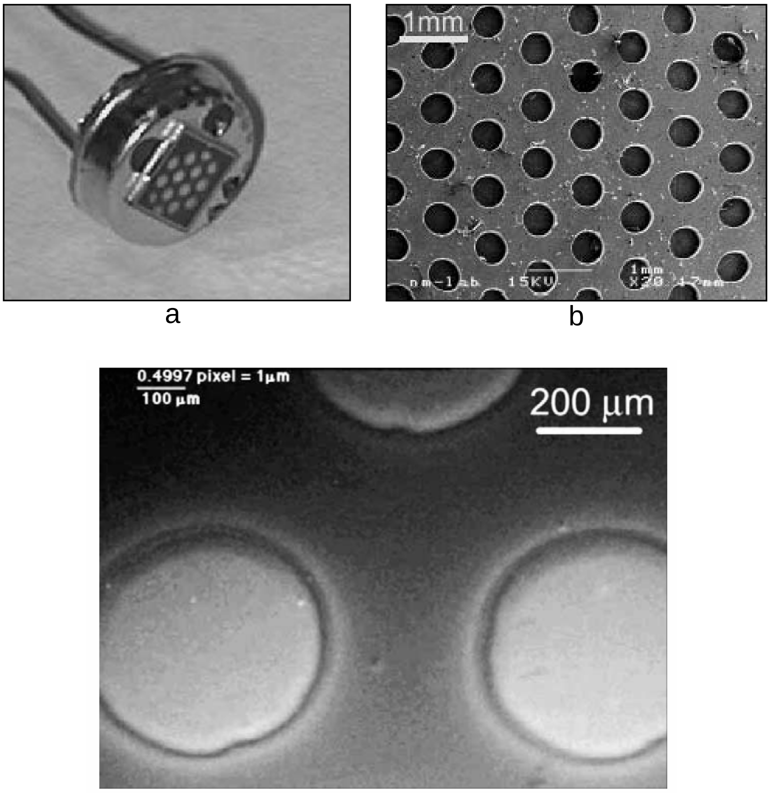

a b

c

Figure 6.9: a) Si PIN diode coated with polka-dot pattern, b) a 0.3 mm thickness mask with 500 μm holes, c) an optical micrograph showing islands of stopping medium deposited on the PIN diode surface. The white rings are interference rings. [Timm04]

6.5 Measurements of the stopping forces in Ge, Ag and Au using "polka-dot" detectors

Ion beam analysis, ion implantation and ion beam modification and hadron oncology rely on accurate stopping data of their targets. Many accepted predictor codes use semi-empirical methods that interpolate from experimental data [Hub90, Zieg85]. Experimental approaches for measuring stopping forces often use self-supporting thin films, which are very difficult to make because of their delicacy. Furthermore, the well known problem of considerable stress in deposited thin films leads to density departures of up to 50% from bulk material. This translates to a considerable difficulty in determining the thickness in terms of number of atoms per unit area. The short range for low energy ions, implies that in many cases, self-supporting foils cannot even be made. In this work, we use a new approach, using "Polka-dot" detector for the measurement of stopping forces of swift heavy ions (0.5 - 1 MeV/amu).

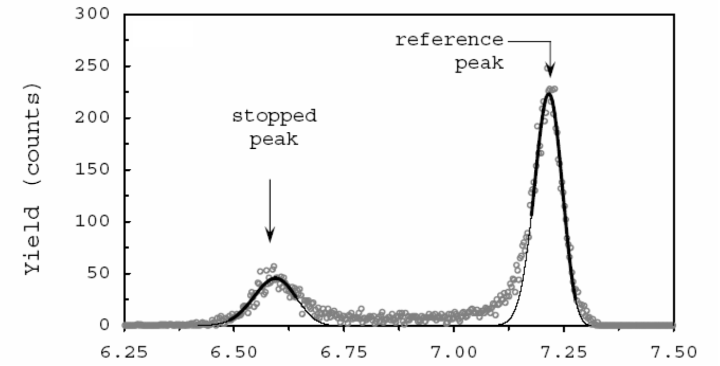

Figure 6.10: Energy spectrum showing the stopped and reference peaks for 7.22 MeV ^{14}N ions incident on the Ge-coated detector (unfilled circles). The skewed Gaussian (Gram-Charlier) fits to the two peaks are overlaid (thin solid black line) as well as the regions of interest used in the fit (thcik solid black line).

The advantages of this approach are:

1. The thin stopping medium is fully supported by Si PIN diode detector;

2. The improvement in controlling of the thickness and uniformity of the coated layer;

3. The use of a polka-dot pattern enables the simultaneous measurement of ions that have passed through the stopping medium and lost energy, as well as those that have been detected directly by the detector without passing through the stopping media.

Figure 6.10 shows the energy spectrum measured for 7.22 MeV ^{14}N ions incident on the Ge-coated detector. Two peaks are observed. The higher energy peak results from ions passing directly into the detector and referred to as the 'reference peak'. The lower energy peak is a result of ions that pass through the full thickness of stopping medium before entering detector. The energy difference between these two peaks, ΔE then gives the stopping cross section ε as:

$$\varepsilon = \frac{\Delta E}{N_x} \tag{6.1}$$

Where, N_x is the atomic density of the stopping medium.

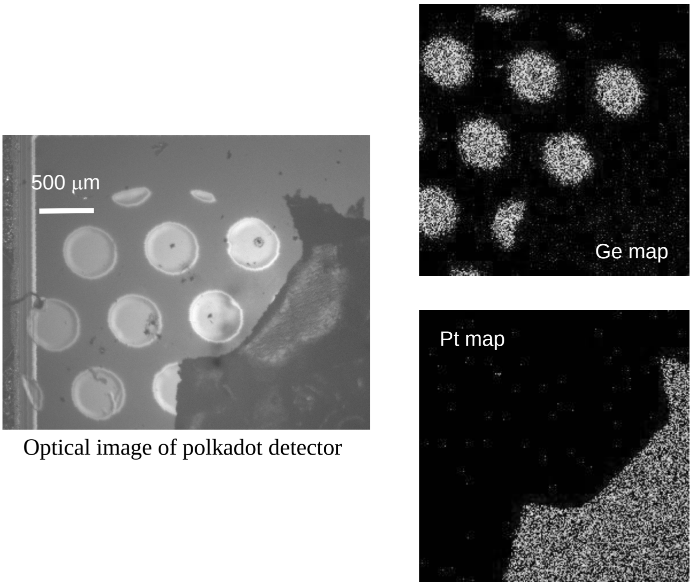

Optical image of polkadot detector

Figure 6.11: Optical image of the polka-dot detector with platinum standdard and RBS elemental maps.

The energy loss measurements were performed for ^{14}C, ^{14}N, ^{16}O and ^{19}F ions in two different labs and details can be found in reference [Weij06]. Here the contribution to this experiment using Nuclear Microscopy via Rutherford Backscattering is described. 2 MeV protons were used for the thickness measurement of the stopping media Ge layer. This thickness measurement was performed last of all because the damage introduced into the detector by the proton beam destroys the resolving power of the detector as described in the section on **beam damage measurement** of this chapter.

The microbeam measurement using 2 MeV protons was carried out on the Ge coated Si Pin-diode detector. Prior to the measurement, a small piece of platinum standard (44.8 μg/cm^2 ± 5%, MicroMatter Co.) was placed onto the polka-dot detector as shown in Figure 6.11 in order to act as a reference to allow absolute measurement of the Ge layer thickness.

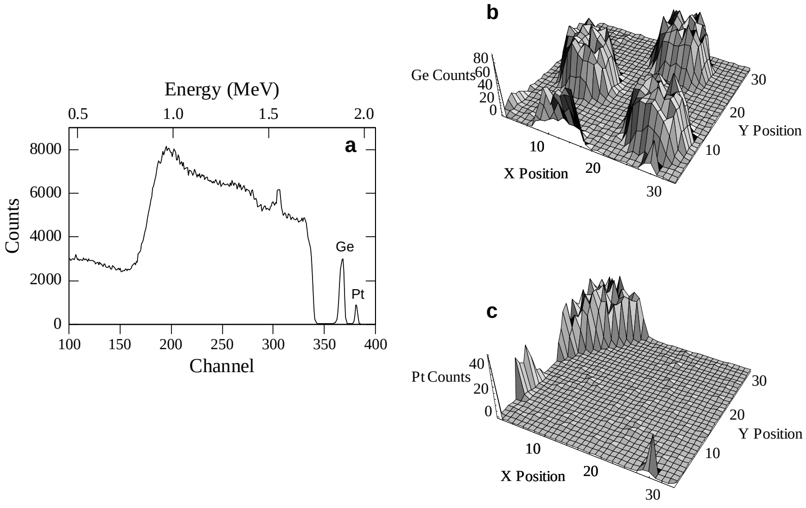

Figure 6.12: a): RBS spectrum obtained from scanning the proton beam over an area including, b) *Pt* distribution contour map, c) *Ge* distribution contour map.

The RBS spectrum (shown in Figure 6.12a) shows well resolved Pt and Ge peaks, which can be directly used for the thickness calculation according to the formulae below:

$$Y_{Ge} = \sigma_{Ge} \cdot \Omega \cdot Q_{p,Ge} \cdot n_{Ge} \cdot t_{Ge} \tag{6.2}$$

$$Y_{Pt} = \sigma_{Pt} \cdot \Omega \cdot Q_{p,Pt} \cdot n_{Pt} \cdot t_{Pt} \tag{6.3}$$

$Q_{p,Ge}/Q_{p,Pt}$ can be then determined by the surface area ratio of Ge and Pt within the scanned area. $n_{Pt}t_{Pt}$ is given for the standard, so $n_{Ge}t_{Ge}$ can be determined. t_{Ge} was calculated to be 311 ± 16 nm (7% error with 5% from the Pt standard). This result shows good agreement with the thickness measurement of Ge layer using alpha energy loss measurements [Timm04]. In order to investigate the uniformity, line scans were performed across the polka-dot as shown in Figure 6.13. It can be seen from this figure that the polka dot is uniform especially in the central region. The edges of the polka dot are sloping which is associated with the edge broadening from the proximity mask used for evaporation.

The thickness measurements for Au and Ag coated polka-dot detectors were carried out in a similar manner.

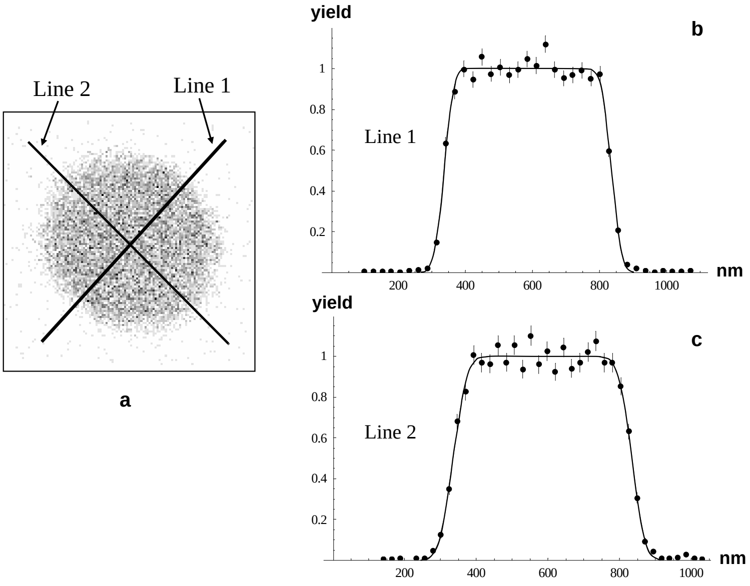

Figure 6.13: a): Map of the backscattered 2 MeV proton signal corresponding to Ge, (b)& (c) Line scans of the Ge signal corresponding to the lines shown in (a).

6.6 Results and conclusions

The proton beam writing facility at the Center for Ion Beam Applications (CIBA) in NUS, with the ability of focusing the ion beam (MeV protons and alpha particles) down to sub-100 nm level, has made it possible for structural imaging of cells at nano-scale level.

The use of Hamamatsu PIN diode acting as a direct STIM particle detector has the advantage of making the imaging process possible in a very confined space, although the detectors were unavoidably damaged by the ion beam.

The nanoSTIM technique has great potential in structural imaging of whole single cells since the spatial resolution of the proton or alpha particle beam passing through the cell is maintained. It is unlikely however that PIXE and RBS techniques can be used simultaneously with nanoSTIM using a pin-diode as a substrate, since the increased beam current density required for these techniques leads to excessive detector damage. In such experiments the use of a thin silicon nitride window as substrate and an off-axis STIM detector would be necessary.

The Si PIN diode is not only useful as STIM detector, when used in a different way, it has also opened up the possibility of making stopping force measurements in extremely thin media.

7 Conclusion and future aspects

This thesis deals with some developments of Nuclear Microscopy physics and their application to biological and materials research. From the research work carried out in this thesis, it is evident that Nuclear Microscopy is a physical method that is very suitable for measuring trace elements in biological tissues and cells in a quantitative way. An important feature is that the tissue thickness can be relatively thick compared to that for electron microscopy. Nuclear Microscopy is also proved to be able to demonstrate structural information about cells at a sub-100 nm level.

In the studies carried out with regard to *atherosclerosis*, we have been able to map the elemental distribution over aortic arterial cross sections encompassing the arterial wall and atherosclerotic lesion and providing direct visualization of elemental changes between them. Quantitative analysis down to the parts per million (wt.) level has enabled us to draw the conclusion that iron is positively correlated with lesion growth and zinc is inversely correlated with the depth of the lesion.

In the *Parkinson's disease* study using primate models, we have shown that Nuclear Microscopy is able to provide information on elemental distribution and concentration to complement the immunochemistry staining results for better understanding of the cause of the disease.

The sensitivity of the techniques discussed in this thesis looks promising for future use in identifying the role of trace elements in free radical damage in biological systems.

Biological matter is one of the most important and diverse classes of materials. Figure 7.1 is a schematic diagram of biological scales illustrating the diversity of biological systems. All living organism from sub-μm sized bacteria to massive trees and mammals, and their products, have the common reliance on genetic information coded onto nanometre scale units of DNA (or in the case of some viruses, RNA), which is expressed in the functionality of nanometer scale proteins. The nature of living organisms would be better understood if available techniques allowed us to provide enough information from a range of different scales (e.g. nano-scale upwards).

Nuclear Microscopy, with a variety of available analytical techniques for the characterization of biological material by determining the distributions of elemental compositions at the cell and sub-cellular level can allow us to infer protein or other biochemical activity. Focused ion beams can also be used for research and therapy by controlling the radiation doses (single ions) to damage specific regions of cells or tissue to study the response to radiation or molecular damage. Focused ion beam can also be used for nanofabrication to create structures for bio-technology applications for example, bio-sensors, biomaterials (drug release devices) and bio-chips.

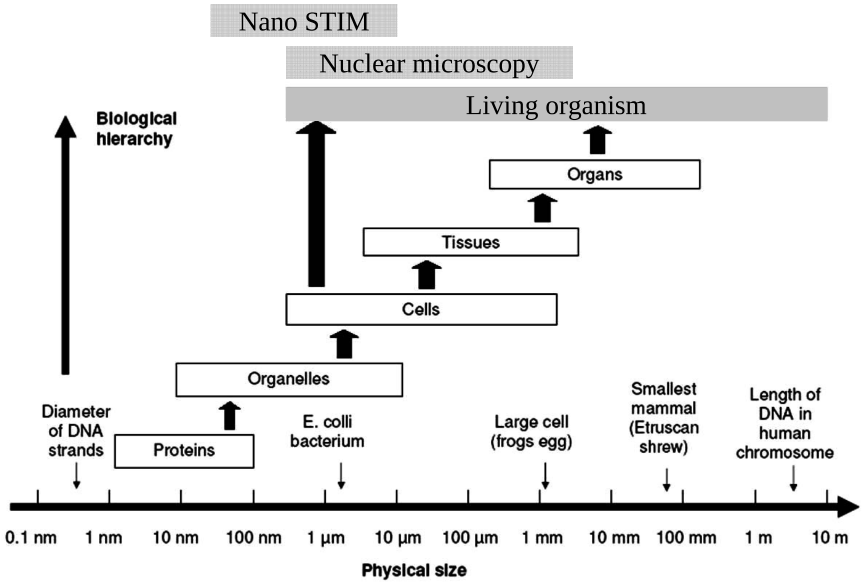

Figure 7.1: Schematic illustration of biological scales and feature sizes analysable with Nano-STIM and nuclear microscopy techniques (after White and Whitlow [White07]).

Current topics in micro/nano-biology which may benefit from the use of focused ion beams include:

- Understanding the fundamental biochemical processes of life:
  1. Causes of disease
  2. Protein and cell function
  3. Structure and synthesis of proteins
  4. Response of organisms to radiation and organic/inorganic toxins

- Manipulating biological processes:
  1. Metabolic function (radiation treatment or therapy)
  2. DNA function (genetic engineering and genomics)

- Exploiting biological processes using nano-technology:
  1. Medical imaging
  2. Bio-materials (implants and drug release devices)
  3. Bio-chips
  4. Bio-sensors
  5. Self-assembling molecules for nano-fabrications

A challenge to using focused ion beams in the biomedical research listed above will be to provide new signals that give nanometer scale spatial information about specific biomolecules. This might be possible by using functionalised nanoparticles, or fluophores as tracers.

Image processing techniques have not been very much explored in connection with Nuclear Microscopy. In this thesis, the use of autocorrelation function (ACF) to study the colocalisation of Ca and P in the atherosclerosis project was investigated. This points to using advanced mathematical techniques to couple image information from nuclear microscopy with other techniques such as atomic force microscopy and confocal microscopy.

The techniques discussed in the thesis are also able to contribute to some of the larger issues facing society. For example: pure potable water is becoming a scarcer resource on this planet, and much effort in Singapore and elsewhere is devoted to water purification. Nuclear Microscopy may be able to help with studying the filters for water purification systems by looking at how undesirable trace elements (e.g. Pb, As etc.) behave in the filtration system.

A Procedure of making 0.5 μm Pioloform film

It is important to reduce the background contribution to the PIXE spectrum to a minimum, but it is essential to have a carrier for the sample. *Pioloform*, known chemically as *polyvinyl butyral*, is perceived to result in a thin film, resulting in less electron scatter for a given film thickness. While not as widely used as some of the other support film materials such as Formvar^{TM} or Parlodion®, this resin is perceived to have a higher thermal stability than either Parlodion or Formvar. It has appeared to be very strong under the ion beam bombardment. It doesn't contain detectable trace elements (by PIXE).

Procedure for making approximately 0.5 μm thick Pioloform film

1. Make up pioloform solution:
   Add 1.25 g (pure grade) pioloform granules to 100ml (high purity) chloroform and allow to dissolve. (Takes about 1-2 hours at room temperature).
   Keep the solution in a sealed clean bottle in the refrigerator.

2. Pour the solution into a Coplin Jar (jar with slits to hold slides in a vertical position). Make sure that the solution is at room temperature. Place slide (BDH super premium microscope slides – 1.0-1.2 mm thick, plain and pre-cleaned) into Coplin jar.
   Lift slides out of jar, and drain the excess liquid from the corner of the slide (for about 3 seconds). Stand the slide to drain at 45^o resting on a lint-free absorber. When dry (a few minutes), store the slides in sealed slides boxes.

3. Making self supporting films using water floatation
   Equipment required: Razor blade, plastic dish filled with doubly distilled water, a wooden handled pointer/needle, and a pair of flat nose angled forceps.
   Score the film on the slide into areas required. Dip the slide into water at an angle of about 45^o. Let the surface tension lift off the pioloform as the slide is gradually lowered into the water; start the process if necessary by teasing the pioloform film until it floats in the water, and can be picked up by the target holder, held by the forceps. It is important that the film is wrapped around the holder for stability.
   If the pioloform appears slack over the hole, it will tighten on drying. Drain

by standing the holder on lint-free tissue at an angle of 45^o, and accelerate the drying using gentle warming if possible.

B Hematoxylin & Eosin staining

Hematoxylin and Eosin (H&E) staining (Figure 4.1b)

Hematoxylin and Eosin stain is a popular staining method in histology. This staining involves using both applications of the basic dye *hematoxylin*, which colors basophilic structures with blue-purple hue, and alcohol-based acidic *eosin*, which colors eosinophilic structure bright pink.

The basophilic structures are usually made up of nucleic acids, such as ribosomes and chromatin-rich cell nucleus, and the cytoplasmatic regions which are rich in RNA. The eosinophilic structures are generally composed of intracellular or extracellular protein. The Lewy bodies and Mallory bodies are examples of eosinophilic structures.

Most of the cytoplasm is eosinophilic. Red blood cells are stained intensely red.

The procedure for H&E staining is as the following:

1. The tissue sections are picked up on gelatin coated slides and air-dried completely
2. Immerse 10% formalin for 5 to 10 minutes
3. The sections were rinsed in two changes of deionized water
4. Immerse in Harris hematoxylin solution for 10 minutes
5. Wash in two changes of deionized water
6. Differentiate in differentiating fluid, which is 70% alcohol with a few drops of HCl, for a few (10 seconds).
7. Wash in deionized water,
8. Blue the section in tap water for 10 to 15 minutes
9. Rinse in deionized water
10. Immerse in 3% eosin solution for 2 to 3 minutes
11. Dehydrate quickly in 90% alcohol, equal parts of absolute alcohol and xylene, followed by three changes of xylene

12. Put a drop of Permount and place a coverslip over the sections

C Nissl staining

Standard Nissl staining protocol (Figure C.1)

The *Nissl* method uses basic aniline to stain RNA blue, and can be used to highlight important structural features of neurons. The Nissl substance (rough endoplasmic reticulum) appears dark blue due to the staining of ribosomal RNA, giving the cytoplasm a mottled appearance. Individual granules of extranuclear RNA are named Nissl granules (ribosomes). DNA present in the nucleus takes on a similar color.

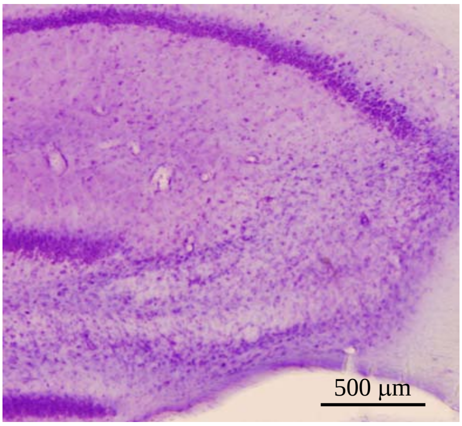

Figure C.1: Image of a Nissl-stained rat brain section showing neuronal bodies in the hippocampus region (picture was kindly provided by Dr Ong Wei Yi).

The protocol is as the following:

1. The tissue sections are picked up on gelatin coated slides
2. They are immersed in 10% formalin for 15 to 20 minutes
3. The sections are then rinsed in two changes of deionized water

4. Slides are transferred into a slide rack, and the rack is left in *Nissl* solution for 15 to 20 minutes
5. Dehydration procedure:
   Dehydrate in 70%, 90%, absolute alcohol 50:50 ethanol, three changes of xylene
6. Put a drop of Permount and place a coverslip over the sections

In order to carry out *Nissl* staining for the sections placed on the Nuclear Microscopy target holders, the steps using xylene need to be skipped. Of course, care needs to be taken during the process in order to avoid losing the supporting film (pioloform film).

D Other publications by the author

1. *Nuclear Microscopy investigation into the trace elemental contents of carotid artery walls of apolipoprotein E deficient mice.* **Ren Minqin**, Huang En, Konstanze Beck, Reshmi Rajendran, Ben J Wu, Barry Halliwell, Frank Watt and Roland Stocker. Nucl. Instr. Meth. B *260*, 240-244, (2007).
2. *Nuclear microscopy measurement of copper in atherosclerosis - Sensitivity and limitations to spatial resolution.* Reshmi Rajendran, **Ren Minqin**, Pan Ning, Benny Tan Kwong Huat, Barry Halliwell and Frank Watt. Nucl. Instr. Meth. B *260*, 136-140, (2007).
3. *Free radical damage in atherogenesis by copper or iron - which is more likely*? Reshmi Rajendran, **Ren Minqin**, Pan Ning, Barry Halliwell and Frank Watt. Biochemical and Biophysical Research Communications *353*, 6-10, (2007).
4. *Zinc supplementation inhibits lipid peroxidation and the development of atherosclerosis in rabbits fed a high cholesterol diet.* Andrew Michael Jenner, **Minqin Ren**, Reshmi Rajendran, Pan Ning, Benny Tan, Frank Watt, Barry Halliwell. Free Radical Biology and Medicine, Vol. *42(4)*, 559-566, (2007).
5. *Zinc supplementation decreases the development of atherosclerosis in rabbits.* **Minqin Ren**, Reshmi Rajendran, Pan Ning, Benny Tan Kwong Kuat, Ong Choon Nam, Frank Watt, Andrew Jenner and Barry Halliwell. Free Radical Biology and Medicine, Vol. *41(2)*, 222-225, (2006).
6. *A nuclear microscopy study of trace elements Ca, Fe, Zn and Cu in atherosclerosis.* F. Watt, R. Rajendran, **M.Q. Ren**, B.K.H. Tan and B. Halliwell. Nucl. Instr. Meth. B *249*, 646-652, (2006).
7. *Iron and copper accumulation in the brain of coxsackievirus-infected mice exposed to cadmium.* NG Ilbäck, U Lindh, **R. Minqin**, G. Friman and F. Watt Environmental Research Vol. *102(3)*, 308-313, (2006).
8. *Hypericin-photodynamic therapy (PDT) using an alternative treatment regime suitable for multi-fraction PDT.* Patricia Soo-Ping Thong, Frank Watt, Min Qin Ren, Puay Hoon Tan, Khee Chee Soo, Malini Olivo. J. Photochem. Photobiol. B *82*, 1-8, (2006).
9. *Selenium and mercury are redistributed to the brain during viral infection in mice.* Nils-Gunnar Ilbäck, Ulf Lindh, Ren Minqin, Göran Friman and Frank Watt. Biological Trace Element Research, Vol. *108 (1-3)*, 215-224, (2005).

10. *A systematic approach to nuclear microscopy of water trees for a large number of field-aged HV cable samples.* M. Ahmed, M. Al-Ohali, M. Garwan, Z. Al-hamouz, K. Al-Soufi, R. Minqin, I Rajta and F Watt. European Transactions on Electrical Power, Vol.*16(1)*, 49-62, (2005).

11. *Hypericin-photodynamic therapy (PDT) using an alternative treatment regime suitable for multi-fraction PDT.* PSP Thong, F Watt, **MQ Ren**, PH Tan, KC Soo and M Olivo. Journal of Photochemistry and Photobiology, B: Biology, (2005).

12. *The protective role of iron chelation and zinc supplements in atherosclerosis induced in New Zealand white rabbits: A nuclear microscopy study.* **MQ Ren**, R Rajendran, N. Pan, BTK Huat and B Halliwell, F Watt. Nucl. Instr. and Meth. B, *231*, 251-256, (2005).

13. *Nuclear Microscopy of diffuse plaques in the brains of transgenic mice.* Reshmi Rajendran, **Minqin Ren**, Gemma Casadesus, Mark.A.Smith, George Perry, En Huang, Wei Yi Ong, Barry Halliwell and Frank Watt. Watt. Nucl. Instr. and Meth. B, *231*, 326-333, (2005).

14. *Investigating the role of calcium and biological trace elements in hypericin photodynamic therapy induced tumor cell death using nuclear microscopy.* PSP Thong, F Watt, **MQ Ren**, KC Soo and M Olivo. Watt. Nucl. Instr. and Meth. B, *231*, 315-320, (2005).

15. *Proton Beam Writing of Erbium Doped Waveguide Amplifiers.* T.C. Sum, A.A. Bettiol, K. Liu, **M.Q. Ren**, E.Y.B Pun, S. Venugopal Rao, J.A. van Kan and F. Watt. Watt. Nucl. Instr. and Meth. B, *231*, 394-399, (2005).

16. *Enhanced low field magnetoresistance of $Al_2O_3-La_{0.7}Sr_{0.3}MnO_3$ composite thin films via a pulsed laser deposition.* L Yan, LB Kong, T Yang, WC Goh, CY Tan, CK Ong, Md Anisur Rahman, T Osipowicz and **MQ Ren**. Journal of Applied Physics, *96(3)*, 1568-1571, (2004).

17. *The mutual diffusion coefficient for (meth) acrylate monomers as determined with a nuclear microprobe.* Christian M Leewis, Peter HA Mutsaers, Arthur M de Jong, Leo J van Ijzendoom, Martien JA de Voigt, **Min Q Ren** and Frank Watt. Journal of Chemical Physics, *120(4)*, (2004).

18. *Proton microprobe analysis of water trees in underground high voltage cables.* M Ahmed, MA Garwan, MA Al-Ohali, Z Hamouz, K, Soufi, **R Minqin**, I Rajta and F Watt. Nucl. Instr. and Meth. B *210*, 548-553, (2003).

19. *Nuclear microscopy of atherosclerotic tissue: A review.* Frank Watt, **MQ Ren**, JP Xie, BKH Tan and B Halliwell, Nucl. Instr. and Meth. B *181*, 431-436, (2001).

20. *Hard metal lung disease — the first case in Singapore.* KL Tan, HS Lee, WT Poh, **Ren Minqin**, Frank Watt, SM Tang, P Eng. Ann Acad Med Singapore, *29*, 521-7, (2000).

21. *Single cell elemental analysis using nuclear microscopy.* **MQ Ren**, PSP Thong, U Kara and F Watt. Nucl. Instr. and Meth. B *150*, 179-184, (1999).

22. *MicroPIXE investigations:Time sequencing studies in degenerative diseases.* F Watt, **MQ Ren** and PSP Thong. International Journal of PIXE, 9 nos 3&4, 189-197, (1999).

23. *Changes in calcium and iron levels in the brains of rats during kainate induced epilepsy.* **Min-Qin Ren**, Wei-Yi Ong, Jagoda Makjanic and Frank Watt. Nucl. Instr. and Meth. B *158*, 418-423, (1999).

24. *Nuclear microscopy in the life sciences at the National University of Singapore. A review.* **Ren MQ**, Thong PS, Makjanic J, Ponraj D, Watt F. Biol Trace Elem Res. Vol. *71-72*, 65-76, (1999).

25. *A Nuclear Microscopic Study of Elemental Changes in the Rat Hippocampus After Kainate-Induced Neuronal Injury.* Ong, Wei-Yi, **Ren, Min-Qin**, Makjanic, Jagoda, Lim, Tit-Meng, Watt, Frank. Journal of neurochemistry, *72*, 1574-1579, (1999).

26. *Nuclear Microscopy Study on Qinghaosu treatment of malaria infected mouse blood.* **MQ Ren**, JK Iyer, UAK Kara and F Watt. IX international congress of parasitology ICOPA IX, Makuhari Messe, Chiba, Japan, 24-28 August, (1998).

27. *Total elemental analysis of biological cells using nuclear microscopy.* **Ren MQ**, Iyer JK, Kara UKA and F Watt. Proceedings of the First Asean Microscopy Conference Nov 27-30, 1997.

28. *PIXE analysis of antinodularizing elements Al, Pb and Bi in nofular cast iron.* SL Feng, **MQ Ren**, M Zhong. Nucl. Instr. and Meth. B *109/110*, 584-586, (1996).

29. *Analysis of the distribution of trace elements in nodular cast iron by SPM.* Feng Songlin, **Ren Minqin**, et al. Instr. and Meth. B *104*, 557-560, (1995).

30. *PIXE and SPM analysis of V, Cr, Cu and Bi in nodular cast iron.* Feng Songlin, Zhong Ming, **Ren Minqin** etc... Instr. and Meth. B *75*, 375-378, (1993).

31. *Distribution of trace elements Cu, Cr and Bi in Nodulcar cast iron by SPM analysis.* Feng Songlin, **Ren Minqin** et al. Nucl. Tech. Vol.16, No7, P416, (1993).

32. *A study of antinodularizing properties of Pb, Bi, Al and Ti in nodular cast iron by SPM.* Feng Songlin, **Ren Minqin** et al. Nucl. Sci. Tech. Vol.*14*, No4, P193, (1993).

33. *Study on trace elements in animals of the deer family with Osteoporosis using ICP.* Feng Songlin, **Ren Minqin** et al. Fen Xi Shi Yan Shi, Vol.*12*, No.6, P69, (1993), (in Chinese).

34. *SPM Applications in Research of Graphite Phase in Nodular Cast Iron.* **Ren Minqin** et al. 3rd China National Conference on microbeam analysis, P493, (1992).

35. *PIXE analysis of graphite phase in nodular cast iron.* Zhong Ming, Feng Songlin, **Ren Minqin** et al. Nucl. Sci. Tech., Vol *13*, No.3, P210, (1992).

36. *An application of PIXE analysis on trace elements of nodular cast iron.* Feng Songlin, **Ren Minqin** et al. Metallury Analysis, Vol.*12*, No.3, P10, (1992), (in Chinese).

37. *The relation between the rubidium content of erythrocyte and ecological environment in Keshan disease area of Sichuan province.* Nianqing, Yan Lingna, **Ren Minqin**, Feng Songlin et al. First International symposium on trace elements and food chain, P36, (1992), China.

38. *Study on Rubidium concentration of different samples from Keshan disease area of Sichuan province.* Inter. Liu Nianqin, **Ren Minqin** et al, Jour. of PIXE, Vol.*2*, No.4, P603, (1992).

39. *Progress in measuring the impurity contents in a* BaF_2 *crystal using the PIXE analysis.* Feng Songlin, **Ren Minqin** et al. International Conference on Activation Analysis and its Applications, P57, Beijing China, (1990).

References

[Ague05] P. Aguer, L.C. Alves, Ph. Barberet, E. Gontier, S. Incerti, C. Michelet-Habchi, Zs. Kerte´sz, A.Z. Kiss, P. Moretto, J. Pallon, T. Pinheiro, J.E. Surle've-Bazeille, Z. Szikszai, A. Verissimo, M.D. Ynsa, Nucl. Instr. and Meth. B **231**, 292 -299, (2005).

[Anne88] R. Anne, J. Herault, R. bimbot, H. Gauvin, G. Bastin and F. Hubert, Nucl. Instr. Meth. B**34**, 295, (1988).

[Bamf66] A.P. Bamford, Transport of Charged Particle Beams, Spon, (1966).

[Bioi04] http://www.bioimagexd.org

[Bird89] J.R. Bird and J.S. Williams, Ion Beam Materials Analysis, Academic Press, (1989).

[Both21] W. Bothe, Z. Phys. **5**, 63, (1921).

[Bray90] T.M. Bray, W.J. Bettger, Free Radic. Biol. Med. **8**, 281, (1990).

[Bree04] M.B.H. Breese, M.A. Rana, T. Osipowicz, E.J. Teo, Phys. Rev. Lett. **93(10)**, 105505, (2004).

[Bree05] M.B.H. Breese, L. Huang, E.J. Teo, P.J.C. King and P.R. Wilshaw, Appl. Phys. Lett. **87**, 211907, (2005).

[Burn83] R.S. Burns, C.C. Chiueh, S.P. Markey, M.H. Ebert, D.M. Jacobowitz, I.J. Kopin, Proc Natl Acad Sci USA, **80**, 4546, (1983).

[Chiu92] C.C. Chiueh, G. Krishna, P. Tulsi, T. Obata, K. Lang, S.J. Huang, D.L. Murphy, Free Radic Biol Med. **13**, 581-583, (1992).

[Chu78] W.K. Chu, J.W. Mayer and M.A. Nicolet, Backscattering Spectrometry, Academic press, (1978).

[Clay86] E. Clayton. PIXAN *The Lucas Heights PIXE analysis computer package* AAEC/M1, (1986).

[Dane99] J. Danesh, P. Appleby, Circulation **99**, 852, (1999).

[Davi79] G.C. Davis, A.C. Williams, S.P. Markey, M.H. Ebert, E.D. Caine, C.M. Reichert, I.J. Kopin, Psychiat Res. **1**, 249, (1979).

[Dean00] R.T. Dean, Redox Rep. **5**, 251, (2000).

[Duvo95] R.C. Duvoisin, J. Sage, Parkinson's Disease: A guide for the patient and family, fourth ed., Lippincott-Raven, New York, (1995).

[Ekte04] de-Ektessabi, A. ; Kawakami, T.; Watt, F., Nucl. Instr. and Meth., B **213**, 590-594, (2004).

[Erem87] V.K . Eremin, E.M. Verbitskaya, A.A . Bribov, V.V. Gusakov,N.B . Strokan, S.M. Tairov, U.Sh. Turebekov and E.V. Shokina, Instr. Exp. Tech. **29**, 1289, (1987). [translated from Pribory i Tekhn. Eksp. 6 (1986) 49].

[Fftp05] http://people.scs.fsu.edu/burkardt/pdf/fftpack5.pdf

[Fran81] C. Francois, J. Nguyen-Legros, G. Percheron, Brain Res. **215**, 317, (1981).

[Froe77] C. Froese-Fischer, The Hartree-Fock method for atoms: a numerical approach, Wiley, New York, (1977).

[Gerl94] M. Gerlach, D. Ben-Shachar, P. Riederer, M.B.H. Youdim, J. Neurochem. **63**, 793, (1994).

[Gile93] W.H. Giles, R.F. Anda, D.F. Williamson, R. Yip, J. Marks, Circulation **87**, 2065-2066, (1993).

[Good87] P.H. Gooda and W.B . Gilboy, Nucl . Instr. and Meth. A **255**, 222, (1987).

[Good92] P.F. Good, C.W. Olanow, D.P. Perl, Brain Res. **593**, 343, (1992).

[Gotz94] M.E.Gotz, G. Kunig, P. Riederer, M.B.H. Youdim, Pharmacol. Ther. **63**, 372, (1994).

[Govl03] P.Govlev, V. Avdeiohitrov, L. Carleh, B. Jahossen, A. Siwek, E.J. van Veldhuizen, L. Werterberg and H.J. Whitlow, Nucl. Instr. Meth. A **500**, 96, (2003).

[Grif99] P.D. Griffiths, B.R. Dobson, G.R. Jones, D.T. Clarke, Brain **122**, 667, (1999).

[Grim84] G.W. Grime, F. Watt, Beam optics of quadrupole probe-forming systems, Adam Hilger Ltd, (1984).

[Grim91] G.W. Grime, M. Dawson, M. Marsh, I.C. McArthur and F. Watt, Nucl. Instr. and Meth. B **54**, 52-63, (1991).

[Hall84] B. Halliwell, J.M. Gutteridge, Biochem. J. **219**, 1, (1984).

[Hall89] B. Halliwell, Free Rad. Biol. Med. **7**, 645-651, (1989).

[Hall99] B. Halliwell, J.M. Gutteridge, Free radicals in biology and medicine. New York Oxford University Press, (1999).

[Hama01] http://sales.hamamatsu.com

[He96] Y. He, P.S.P. Thong, T. Lee, S.K. Leong, C.Y. Shi, P.T. Wong, S.Y. Yuan, F. Watt, Brain Res. **735**, 149, (1996).

[Henn96] B. Hennig, M. Toborek, C.J. McClain, Nutrition **12**, 711, (1996).

[Hill84] J.M. Hill, R.C. Switzer, Neuroscience **11(3)**, 595, (1984).

[Hub90] F. Hubert, R. Bimbot, H. Gauvin, Atom. Data Nucl. Data Tables **46**, 1, (1990).

[Jenn98] P. Jenner, Mov. Disord. (suppl) **13**, 24, (1998).

[John70] T.B.Johansson, R. Akselsson and S.A.E. Johansson, Nucl. Instr. And Meth. **84**, 141-143, (1970).

[John88] Johansson SAE and Cambell JL, PIXE: A Novel Technique for Elemental Analysis, Wiley, Chichester, 1988.

[Kost74] R.M. Kostrzewa, D.M. Jacobowitz, Pharmacol Rev. **26**, 199, (1974).

[Lang96] J.W. Langston, Neurology **47**, [Suppl 3], S153-S160, (1996).

[Lind63] J. Lindhard, M. Scharff and E.M. Schiott, K. Dan. Vidensk. Selsk., Mat. Fys. Medd. **33**, No14, (1963).

[Lynn73] P.A. Lynn, An introduction to the analysis and processing of signals, Macmillan, London, P85, 1973.

[Lusi00] A.J. Lusis, Nature **407**, 233, (2000).

[Maet99] M. Maetz, J. Wojtek, Przybylowicz, J. Mesjasz-Przybylowicz, A Schûler, K. Traxel, Nucl. Instr. and Meth. B **158**, 292 - 298, (1999).

[McMa60] J.F.A. McManus, R.W. Mowry, Staining methods for iron. In: Staining Methods-Histologic and Histochemical. pp. 195-197, (1960).

[Marw75] A.D. Marwick, P. Sigmund, Nucl. Instr. and Meth. **126**, 317, (1975).

[Maxw89] J.A. Maxwell, J.L. Campbell and W.J. Teesdale, Nucl. Instr. And Meth. B **43**, 218, (1989).

[May97] M. Mayer, SIMNRA User's Guide, Report IPP **9/113**, Max-Planck-Institut für Plasmaphysik, Garching, Germany, (1997).

[Meye71] L. Meyer, Phys. Stat. Sol. (b) **44**, 253, (1971).

[Moli48] G. Moliere, Z. Naturforschung, A **3**, 78, (1948).

[Ong99] Ong, W.Y., Ren, M.Q., Makjanic, J.H., Lim, T.M., Watt, F., Journal of Neurochem. **72**, 1574-1579, (1999).

[Over83] J.C. Overley, R.C. Connolly, G.E. Seiger, J.D. MacDonald and H.W. Lefevre, Nucl. Instr. And Meth. **218**, 43, (1983).

[Para01] http://www.paraview.org

[Park17] J. Parkinson, An Essay on the Shaking Palsy. Whittingham and Rowland for Sherwood. Neely and Jones, London, (1817).

[Ponk98] P. Ponka, C. Beaumont, D.R. Richardson, Semin. Hematol. **35**, 35, (1998).

[Ponr99] D. Ponraj, J. Makjanic, P.S.P. Thong, B.K.H. Tan, F. Watt, FEBS Lett. **459**, 218, (1999).

[Poss97] Poss KD, Tonegawa S. Proc Natl Acad Sci USA. **94**, 10925-10930, (1997).

[Ren99] Ren, M.Q., Ong, W.Y., Makjanic, J., Watt, F., Nucl. Instr. and Meth. B **158**, 418-423, (1999).

[Ren03] Ren Minqin, Frank Watt, Benny Tan Kwong Huat and Barry Halliwell, Free Radic. Biol. Med. **34(6)**, 746-752, (2003).

[Ren05] M.Q. Ren, R. Rajendran, N. Pan, B.K.H. Tan, W-Y Ong, F. Watt, B. Halliwell, Free Rad. Biol. Med., **38**, 1206-1211, (2005).

[Ren06] Minqin Ren, Reshmi Rajendran, Pan Ning, Benny Tan Kwong Huat, Ong Choon Nam, Frank Watt, Andrew Jenner and Barry Halliwell, Free Rad. Biol. Med., **41**, 222-225, (2006).

[Ross99] R. Ross, N. Engl. J. Med., **340**, 115, (1999).

[Rossi00] E. Rossi, B.M. McQuillan, J. Hung, P.L. Thompson, C. Kuek, J.P. Beilby, Stroke **31**, 3015, (2000).

[Rsb02] http://rsb.info.nih.gov/ij/

[Ryt06] S.W. Ryter, J. Alam, A.M. Choi, Physiol. Rev. **86**, 583-650, (2006).

[Sal95] J.T. Salonen, H. Korpela, K. Nyyssonen, E. Porkkala, T.P. Tuomainen, J.D. Belcher, D.R. Jacobs Jr., R. Salonen, J. Intern. Med. **237**, 161, (1995).

[Schi98] H.M. Schipper, R. Vininsky, R. Brull, L. Small, J.R. Brawer, Exp. Neurol. **152** 188, (1998).

[Scot63] W.T. Scott, Rev. Mod. Phys. **35(2)**, 231, (1963).

[Seal83] R.M. Sealock, A.P. Mazzolini and G.L.F. Legge, Nucl. Instr. And Meth. **218**, 217, (1983).

[Seat97] T.A. Seaton, J.M. Cooper, A.H.V. Schapira, Brain Res., **777**, 110-118, (1997).

[Gore07] S.Gorelick, T. Ylimaki, T. Sajavaara, M. Laitinen, A. Sagari A.R. and H.J. Whitlow, Nucl. Instr. Meth. B (in press), (2007).

[Sig74] P. Sigmund, K.B. Winterbon, Nucl. Instr. and Meth. **119**, 541, (1974).

[Sig78] P. Sigmund, J. Heinemeier, F. Besenbacher, P. Hvelplund, H. Knudsen, Nucl. Instr. and Meth. **150**, 221, (1978).

[Sim05] A. Simon, G. Kalinka, Nucl. Instr. and Meth. B **231**, 507-512, (APR 2005).

[Sing87] T.P. Singer, N. Castagnoli Jr, R.R. Ramsay, A.J. Treor, J Neurochem. **49**, 1-8, (1987).

[Slic03] http://www.slicer.org

[Smit92] C. Smith, M.J. Mitchinson, O.I. Aruoma, B. Halliwell, Biochem. J. **286**, 901, (1992).

[Sofi88] E. Sofic, P. Riederer, H. Heinsen, H. Bechmann, G.P. Reynolds, G. Hebenstreit, M.B.H. Youdim, J. Neural. Trans. **74**, 199, (1988).

[Sofi92] E. Sofic, K.W. Lange, K. Jellinger, P. Riederer, Neurosci. Lett. **142**, 128, (1992).

[Stad04] N. Stadler, R.A. Lindner, M.J. Davies, Arterio. Thromb. Vasc. Biol. **24**, 949-954, (2004).

[Sull89] J.L. Sullivan, Am. Heart J. **117**, 1177, (1989).

[Sun04] Sun, Feng; Casse, Didier; Van Kan, Jeroen Anton; Ge, Ruowen; Watt, Frank. Tissue Engineering, **10**, 267-272, (2004).

[Thon96] PSP Thong, M. Selley and F. Watt, Cellular and Molecular Biology, **42(1)**, 103-110, (1996).

[Thon97] P.S.P Thong, Y. He, T. Lee, F. Watt, Nucl. Instr. and Meth. B **130**, 460, (1997).

[Thon99] Thong, P.S.P., Watt, F., Ponraj, D., Leong, S.K., He, Y., Lee, T., Nucl. Instr. and Meth. B **158**, 349-355, (1999).

[Timm04] H. Timmers, K. Stenstrom, M Graczyk and H.J. Whitlow, Nucl. Instr. and Meth. B **219-220**, 263-267, (2004).

[Udal05] C.N.B. Udalagama, A.A. Bettiol, J.A. van Kan, E.J. Teo, M.B.H. Breese, T. Osipowicz and F. Watt, Nucl. Instr. and Meth. B **231**, 389-393, (2005).

[Van03] JA van kan, AA Bettiol and F Watt, F. Mater. Res. Soc. Symp. Proc. 777, T2.1.1., (2003)

[VanK03] J.A. van Kan, A.A. Bettiol and F. Watt, Applied Physics Letters **83**, 1629-1631, (2003).

[VanK04] Abstract of third international conference on Nanoimprint Nanoprint Technology, Vienna, Austria, (2004).

[VanK04] J.A. van Kan, P.G. Shao, P. Molter, M. Saumer, A.A. Bettiol, T. Osipowicz and F. Watt, Nucl. Instru. Meth. B **231**, 170-175, (2005).

[Wang98] Wang LJ, Lee TS, Lee FY, Pai RC, Chau LY. Am J Pathol. **152**, 711-720, (1998)

[Watt94] F. Watt, I. Orlic, K.K. Loh, C.H. Sow, P. Thong, S.C. Liew, T. Osipowicz, T.F. Choo, S.M. Tang, Nucl. Instru. Meth. B **85**, 708-715, (1994).

[Watt95] F. Watt, Nucl. Instr. and Meth. B**104**, 276-284 (1995).

[Watt01] F. Watt, M.Q. Ren, J.P. Xie, B.K.H. Tan, B. Halliwell, Nucl. Instr. and Meth. B **181**, 431-436, (2001).

[Watt03] F. Watt, J.A. van Kan,I, Rajta, A.A. Bettiol, T.F. Choo, M.B.H. Breese, T. Osipowicz, Nucl. Instr. and Meth. B **210**, 14-20, (2003).

[Watt05] F. Watt, A.A. Bettiol, J.A. van Kan, E.J. Teo and M.B.H. Breese, International Journal of Nanoscience, **4**, No.3, 269-286, (2005).

[Watt06] F. Watt, Reshmi Rajendran, Minqin Ren, B.K.H. Tan and Barry Halliwell, Nucl. Instr. and Meth. B **249**, 646-652, (2006).

[Weij06] TDM Weijers-Dall, H. Timmers, K. Stenstrom, P. Persson, A. Pergjegjaj, X. Wang, M. Graczyk, T. Osipowicz, M.Q. Ren, D.J. O'Connor, H.J. Whitlow, Nucl. Instr. and Meth. B **251**, 352-360, (2006).

[White07] D.J. White, H.J. Whitlow, *Nanoscale engineering in biosciences*, in *Ion Beam Methods in Nanoscience and Technology.* Ed. by H.J. Whitlow, et al. to be published by Springer (2007).

[Whit98] H.J. Whitlow, S.J. Roosendaal, E.l. Bouanani, R. Ghetti, R.N. Johnston, B. Jakobsson, R. Hellborg, H. Petersson, P. Omling, Z.G. Wang, Nucl. Instr. and Meth. B **135**, 523-531, (1998).

[Whit07] H.J. Whitlow, Minqin Ren, Jeroen A. van Kan, Frank Watt and Dan White, Nucl. Instr. and Meth. B **260**, 28-33, (2007).

[Wint70] K.B. Winterbon, P. Sigmund and JB Sanders, Spatial distribution of energy deposited by atomic particles in elastic collisions, Mat. Fys. Medd. Dan. Vid. Selsk. **37**, No 14, (1970).

[Winz00] T. Winzell, Low and high energy ion beams in nanotechnology, Lund Institute of Technology, p29, (2000).

[Yama84] H. Yamamoto, S. Hatakeyama, T. Norimura and T. Tsuchiya, Radioisotopes **33**, 864, (1984).

[Youd93] M.B.H. Youdim, D. Ben-Shachar, P. Riederer, Trends Pharmacol. Sci., **8**, 45, (1993).

[Zhan07] F. Zhang, J.A. van Kan, S.Y. Chiam and F. Watt, Nucl Instr and Meths B, (in Press) 2007

[Zhan05] Y. Zhang and H.J. Whitlow, MeV ion beam modification of materials, in: Electrostatic Accelerators (ed.) R. Hellborg (Springer,Berlin, 2005) p507

[Zieg85] JF Ziegler, The Stopping and Range of Ions in Matter volumes 2 - 6, Pergamon Press, 1977-1985, http://www.srim.org/